Materials Advances

REVIEW

Check for updates

Core–shell nanostructures for better thermoelectrics

Rafiq Mulla [ID] and Charles W. Dunnill [ID]*

Substantial attempts have been made in recent decades to enhance the thermoelectric performance and find new materials. The inherent complexity and strong correlation between the electronic and thermal parameters of the materials pose serious challenges to enhance their thermoelectric performance. Recent studies on "core–shell" nanostructures and their nanocomposites have indicated that the new strategy of creating such structurally engineered materials can help in several ways to achieve high thermoelectric performances by breaking the strongly coupled electronic and thermal parameters. Furthermore, the dependence of the Seebeck coefficient and electrical conductivity on the carrier concentrations can be altered through the core–shell structure induced energy filtering effects. This review focuses on the experimental evidence and theoretical predictions in the context of core–shell nanostructures and their composite thermoelectric materials. It also highlights the fabrication processes and concepts used to produce these novel core–shell nanostructures.

1. Introduction

Thermoelectric phenomenon, which involves the conversion of thermal energy into electrical energy, is expected to play an important role in meeting the energy needs of the future.[1] Conversely, it can also provide a method for heating and cooling materials.[2] Therefore, thermoelectric devices can be utilized for both electricity generation and cooling/heating applications.[3] In particular, thermoelectric generators harvesting electricity from waste heat offer a promising option to generate clean and alternative energy.[4] There is also a growing interest in converting industrial waste heat into hydrogen fuel using water splitting units[5,6] powered by thermoelectric generators[6–9] as well as a growing demand for wearable and flexible power sources due to the emergence of artificial intelligence.[10,11] In this context, thermoelectric generators can be promising candidates to develop self-powered wearable devices, where these generators can power such smart devices by generating electricity from human body heat.[10] The efficiency (η) of thermoelectric devices for electric power generation is defined as the ratio of output electrical power (P)

Energy Safety Research Institute, Swansea University, Bay Campus, Fabian Way, Swansea SA1 8EN, UK. E-mail: c.dunnill@swansea.ac.uk

Rafiq Mulla

Dr Rafiq Mulla received his Masters degree in Physics with specialisation in Condensed Matter Physics. He was awarded his PhD from the Karnatak University Dharwad, where he studied thermoelectric materials under the supervision of Prof. M. K. Rabinal. Subsequently, he joined Energy Safety Research Institute, Swansea University to work with Dr Charlie Dunnill as a Postdoctoral Researcher, where he is working on developing low-cost economical material fabrication methods.

thermoelectric materials and

Charles W. Dunnill

Dr Charles W. Dunnill is a senior lecturer at Swansea University specializing in sustainable hydrogen generation technology. He was awarded his PhD from Glasgow University in Nanomaterials before taking up a postdoctoral researcher post at University College London, where he was a Ramsay Fellow. Charlie advocates and researches the use of hydrogen as the perfect universal energy carrier to store, transport, and decouple renewable energy supplies from demand for energy, as well as photocatalytic water splitting as a method for solar energy harvesting.

to the thermal power (Q) supplied to the device:[12]

$$\eta = \frac{P}{Q} = \frac{\Delta T}{T_h}\left[\frac{\sqrt{1+zT}-1}{\sqrt{1+zT}+\dfrac{T_c}{T_h}}\right] \quad (1)$$

where T_h is the hot-side temperature, T_c is the cold-side temperature and $\Delta T = T_h - T_c$ is the temperature difference. The term zT is known as "figure of merit", which is used as a performance indicator of thermoelectric materials:

$$zT = \frac{S^2\sigma T}{\kappa} \quad (2)$$

where S, σ, κ, and T are the Seebeck coefficient, the electrical conductivity, the thermal conductivity, and the absolute temperature.[13] Eqn (1) and (2) show that the thermoelectric materials with high zT values can result in high device efficiency (η). The zT can be enhanced by improving the electronic (S and σ) and reducing thermal transport ($\kappa = \kappa_c + \kappa_l$; κ_c and κ_l are the electronic and thermal contributions to the total thermal conductivity) properties of materials, yet, the realization of a high zT is rather complicated because of the strong interactions between these transport parameters, as illustrated in Fig. 1.[14]

Two classical trade-off relationships exist between the above three parameters: (i) a trade-off between S and σ in materials that can give a maximum "thermoelectric power factor" ($S^2\sigma$) and (ii) a trade-off between σ and κ because the parameter σ is also responsible for increasing κ by electronic contribution to the thermal conductivity ($\kappa = \kappa_c + \kappa_l$).[14] These aspects indicate that the semiconductors are quite suitable for the applications. Several bulk semiconductors with optimized zT have been developed in the past several years, however, the zT values are not high enough.[2] Therefore, except in a limited number of cases, the working efficiencies of the devices have fallen short of the targets essential for them to be used largely.[2]

Accordingly, the interest was focused on improving the performance of materials. Hicks and Dresselhouse published a first-ever theoretical model in 1993, predicting significant enhancements in zT by two-dimensional quantum wells.[2] They have shown that the Seebeck coefficient could be increased and the thermal conductivity could be suppressed, simultaneously.
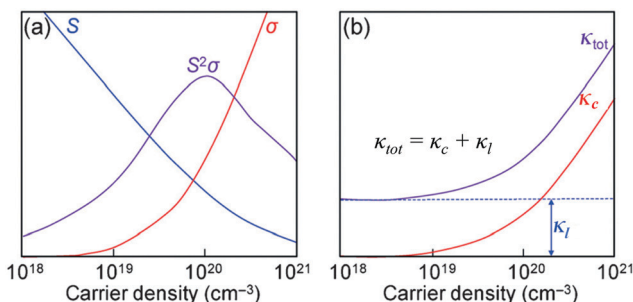

Fig. 1 (a) Illustrations of the trade-off relationship between the Seebeck coefficient (S) and electrical conductivity (σ). (b) Variation in the thermal conductivities (κ_c and κ_{tot}) as a function of the carrier density. Reproduced with permission from ref. 14, Copyright 2015 Wiley-VCH.

These predictions on thermoelectric enhancements were experimentally demonstrated by Venkatasubramanian *et al.* who reported the highest room-temperature zT of about 2.4 from nanoscale layers.[2] The enhanced zT was the result of the enhanced Seebeck coefficient and suppressed thermal conductivity in those nanostructures. Hicks and Dresselhouse further predicted the enhancements in zT of all the three low-dimensional structures such as thin-films (2D), nanowires (1D), and also quantum dots (0D).[15] In such low-dimensional structures, modifications in the band structure, energy levels, and the density of states (DOS) of electrons play a major role in enhancing zT. Since then, most of the research activities have been focused on superlattices,[16–18] nanosheets,[19–21] nanowires,[22–24] nanoribbons,[25,26] mono/bilayer materials,[27–29] nanocomposites,[30,31] and so on.[32,33] Similarly, a strategy that could lead to an economical thermoelectric material with enhanced efficiency is to fabricate nanostructured bulk materials.[13] This approach can reduce the thermal conductivity of the material by disrupting the crystal's phonon transport.[13] Over the past few decades, great progress has been achieved in finding new and structural thermoelectric materials. Materials such as $(Bi,Sb)_2(Te,Se)_3$,[34] $Pb(Te,Se,S)$,[35,36] $SnSe$,[37–39] $SiGe$,[40,41] Cu_2-(Se,S,Te),[42–47] clathrates,[48] skutterudites,[49] Heusler alloys[50,51] are some of the high zT candidates.[12] Recent studies also show that significant enhancements in zT are achieved by reducing the thermal conductivity *via* the introduction of additional phonon scattering regions in bulk materials.[52] All these new thermoelectric materials have the potential to improve the performance level of modern thermoelectric devices.[1,53]

Recently, some studies have introduced a fascinating class of materials to the thermoelectrics known as "core–shell" structures. These core–shell structures have shown promising thermoelectric improvements due to their special physical structure. This review focuses on the studies on core–shell structures and discusses recent developments and their advantages for thermoelectrics.

2. Core–shell structures

Core–shell structures are a type of biphasic materials composed of an inner core material uniformly enveloped by an outer shell of one or more layers of other materials.[54,55] Two common structures of core–shell materials are the core–shell nanoparticles and core–shell nanowires/nanorods, as schematically illustrated in Fig. 2. Core–shell nanostructures are usually obtained from colloidal synthesis strategies (Fig. 3), some of the common growth schemes are (a) direct nucleation and growth of the shell layer onto pre-formed cores, (b) shell layer growth after chemical activation of the core, (c) sacrificial redox replacement of the core outer region/surface; and (d) one-pot self-controlled growth of core and shell.[55] Recent developments in material synthesis techniques have made the preparation of various kinds of core–shells such as metal–metal, metal–semiconductor, and semiconductor–semiconductor combinations possible.[56]

These core–shell structures possess multifunctional properties through integrating two different materials into one entity.[57]
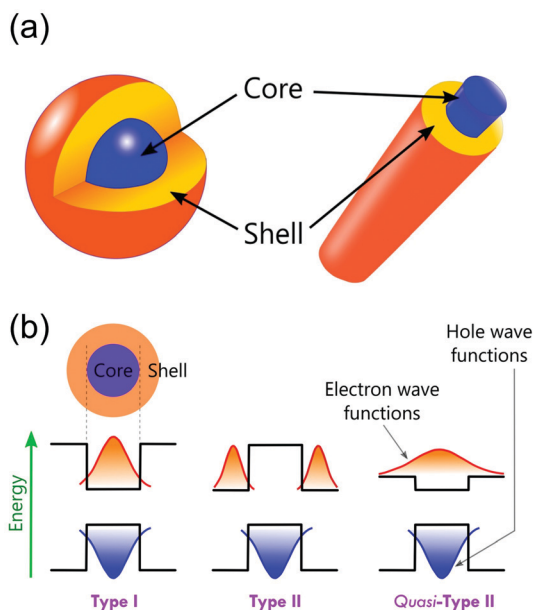
(a)

(b)

Fig. 2 (a) Schematic of core–shell nanoparticle and core–shell nanowire/nanorod. (b) Schematic representations of energy band diagrams and carrier localization in different types of core–shell structures.

Fig. 3 Schematic of different mechanisms that form core–shell heterostructures. (a) Direct nucleation and growth of the shell layer onto preformed cores. (b) Shell layer growth after chemical activation of the core. (c) Sacrificial redox replacement of the core outer region/surface. (d) One-pot self-controlled growth of core and shell. Reproduced with permission from ref. 55, Copyright 2008 Wiley-VCH.

Therefore, they are widely studied and used in various applications such as catalysis,[58–63] electronics,[64,65] biomedical applications,[66–68] photoluminescence,[69–72] sensors,[73] piezo-electrics,[74,75] magnetic applications,[76–78] energy storage,[79,80] solar cells,[81–83] and CO_2 capture.[84–86]

Core–shell materials offer additional electronic modifications due to band-edge alignment at the interface between the core and shell.[87,88] These are classified into Type-I and Type-II as shown

schematically in Fig. 2b. In Type-I, the charges are localized within the core region as the shell with an energy band-gap wrapping that of the core.[87] In Type-II, the band-gap alignments are staggered, resulting in the allocation of the carriers in the core as well as the shell.[87] Type-II can have other possible band-gap alignments known as Quasi-Type-II structures. This occurs when the band offsets are small in type-II structures, resulting in a delocalized charge carrier over the entire nanostructure while the other carrier is confined in either the core or the shell.[87] Thus, the effective band-gaps of the core–shell nanostructures can be precisely controlled by choosing suitable core and shell materials, which results in the modifications of the electronic and optical properties of core–shell nanostructures.[89,90]

3. Core–shell structures for thermoelectrics

Different well-known strategies such as the design of alloys,[91] complex crystal structuring,[92] impurity doping,[93] resonant level doping,[94,95] heavy element compounds,[96] nanostructured materials,[97] and so on, are in use for the enhancement of thermoelectric performance. Most of these approaches mainly focus on reducing thermal conductivity and increasing the Seebeck coefficient. For illustration, alloys, heavy element compounds, complex crystals, nanostructured materials have a significant role in reducing thermal conductivity. Similarly, the Seebeck coefficient and the electrical conductivity can be tuned by impurity doping, resonant level doping, and nanostructured materials.[93,94,97–99]

The Seebeck coefficient can be expressed as:[95,100]

$$S = \frac{\pi^2 k_B^2 T}{3q} \left(\frac{d[\ln \sigma(E)]}{dE} \right)_{E=E_f} \quad (3)$$

$$S = \frac{\pi^2 k_B^2 T}{3q} \left(\frac{1}{n} \frac{dn(E)}{dE} + \frac{1}{\mu} \frac{d\mu(E)}{dE} \right)_{E=E_f} \quad (4)$$

where k_B, q, σ, T, E, and E_f are Boltzmann constant, charge of the carrier, electrical conductivity, temperature, electron energy, and the Fermi energy, respectively. The terms, $n(E)$ and $\mu(E)$ are the energy-dependent carrier density and mobility, respectively.[100] Therefore, the Seebeck coefficient can be enhanced by two mechanisms: (i) increasing the density of states (DOS) near the Fermi level and (ii) increasing the energy dependence of $\mu(E)$ using energy filtering effects. Increasing DOS can be effectively achieved from resonant level doping or band engineering. Resonant levels appear through interactions between the dopants and the host. The dopants with similar electronic configurations as the host atoms are usually chosen to achieve changes in the DOS.[94] Band engineering to converge the bands is another effective approach that results in the high Seebeck coefficients due to energy filtering (or carrier filtering) effects.[100,101]

Thermoelectric studies in the literature on core–shell structures indicate that these novel structurally engineered materials can be used mainly in three different ways as shown in Fig. 4 such as (i) core–shell nanostructures as building blocks, (ii) core–shell

(a)　　　　(b)　　　　(c)

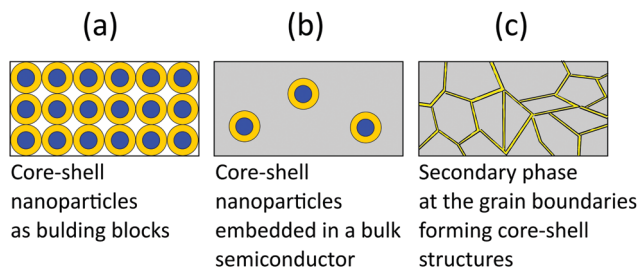| Core-shell nanoparticles as building blocks | Core-shell nanoparticles embedded in a bulk semiconductor | Secondary phase at the grain boundaries forming core-shell structures |

Fig. 4 Different ways of utilizing core–shell structures for thermo-electrics.

nanostructures in bulk semiconductors, and (iii) secondary phase at grain boundaries. The energy filtering effects are well observed from these core–shell structures as they introduce multiple potential barriers. These potential barriers enable selective scattering of low-energy carriers and only allow high energy carriers, as they can cross these barriers.[100] A schematic illustration in Fig. 5 shows the carrier filtering effect due to band alignment at the interface between two different semiconductors (Bi_2Te_3 and Bi_2Se_3).[14,102]

Further, the electronic modifications due to band-edge alignment at the interface between the core and shell can also play an important role in minority carrier filtering (Fig. 5(b)) and help achieve higher Seebeck coefficients.[103,104] When designing a thermoelectric material, either the core or the cell material can be carefully chosen to act as a minority carrier blocking region. Such structures essentially reduce the mobility of the minority charge carrier and lighten the effect of the
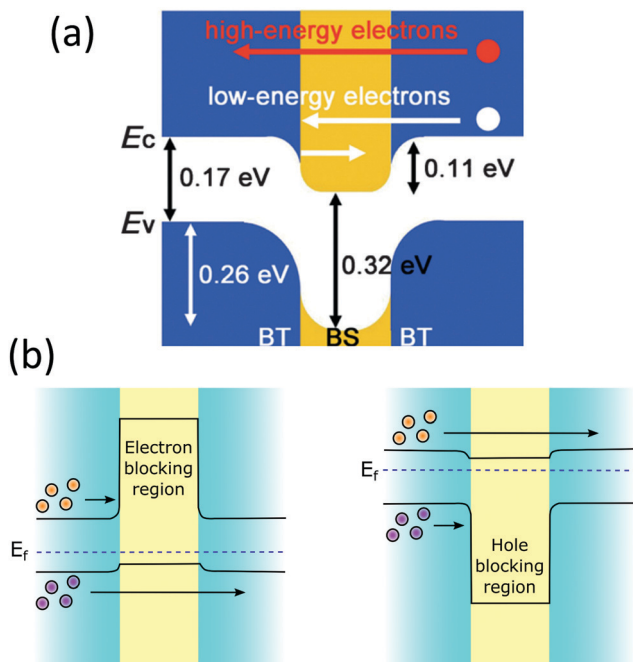

Fig. 5 (a) Schematic band alignment at the interface of bismuth telluride (BT) and bismuth selenide (BS). Reproduced with permission from ref. 102, (Copyright 2013 Wiley-VCH). (b) Schematic energy band diagrams showing electron-blocking and hole-blocking regions.

minority carriers on the Seebeck coefficient.[104] Especially in the narrow band-gap thermoelectric materials, the minority carriers' effect is detrimental to their thermoelectric performance. For illustration, the net Seebeck coefficient (S) of a material with mixed carrier contributions is expressed as[105]

$$S = \frac{S_p \mu_p p + S_n \mu_n n}{\mu_p p + \mu_n n} \qquad (5)$$

where S_p, S_n, μ_p, μ_n, p, and n are the positive Seebeck coefficient, negative Seebeck coefficient, hole mobility, electron mobility, hole density, and electron density, respectively. The deterioration of net S due to minority carriers can be avoided by introducing suitable barriers which can block minority carriers, whereas the other type carriers are less affected.[103] Therefore, by introducing heterojunctions with help of core–shell structures, suitable band-edge alignments can be created at the interface between the core and shell that can preferentially block minority carriers, as a result, a high Seebeck coefficient can be maintained.[103]

In addition, the presence of interfaces in core–shell type materials can act as thermal barriers and work as scatterers of long-wavelength phonons, resulting in the reduction of thermal conductivity but increase the Seebeck coefficient.[106] The presence of multiphase provides an opportunity to have a unique carrier transport behaviour that can decouple electron and phonon transport at the interfaces.[53] This helps reduce thermal conductivity without much loss in the electrical conductivity of the materials.[53] As the thermal conductivity of a material (κ) relies on the charge carriers (κ_c) as well as the lattice vibrations (κ_l) of the crystal,

$$\kappa = \kappa_c + \kappa_l \qquad (6)$$

it can be reduced by controlling either κ_c or κ_l or both. According to the Wiedemann–Franz law, the first term, κ_c is related to electrical conductivity (σ), Lorentz number (L) and temperature (T), expressed as:[53]

$$\kappa = L\sigma T + \kappa_l \qquad (7)$$

Any reduction in κ_c will reduce the electrical conductivity (σ). Instead, κ_l should be reduced without affecting the electronic transport in order to see overall improvements in the thermoelectric performance, zT. However, the lattice contribution cannot be reduced significantly without the negative effects on electronic transport, and in general, it cannot reach below the amorphous limit.[53] Here, multiphase crystal structures such as core–shell type materials can have the exception from such a constraint and possess ultralow thermal conductivity without losing other properties if materials are designed carefully with suitable phases. Also, however, the energy filtering effect has a positive impact on the increase of the Seebeck coefficient, but the reduction of effective mass after the reduced carrier concentration can be detrimental to the increase of the Seebeck coefficient. Therefore, optimization of thermoelectric performance requires a compromise between all the electronic and thermal parameters and their resulting properties to achieve overall improvements.

3.1. Core–shell nanostructures as building blocks

Nanoparticles and nanowires have been attractive materials for thermoelectrics due to their special electrical properties as compared to their bulk counterpart. Further improvements in their thermoelectric performance can be expected with special physical structures in the form of core–shell configurations. Therefore, several research studies have been focused on the fabrication of different core–shell nanostructures for thermo-electric applications.[107] Use of core–shell nanoparticles/nano-wires as building blocks of thermoelectric composites is an interesting strategy employed in several studies.[107] In such materials, the advantages of core–shell structures can be more significant as each particle of the material can possess special electrical features due to their core–shell configurations. The bottom-up growth of nanocrystals is a convenient strategy to form core–shell nanoparticles, which also provides access to a three-dimensional composition control.[107,108] In recent work, Ibáñez et al. reported a high-yield and scalable colloidal syn-thetic route based on the bottom-up assembly to obtain PbTe@PbS core–shell nanoparticles.[107] The nanocomposites of these core–shell nanoparticles have shown up to 10 times higher electrical conductivities than the pure PbTe and PbS nanomaterials due to synergistic nanocrystal doping effects. As illustrated by Fig. 6, the PbS shell on PbTe forms a quasi-type-II heterojunction which assists the selective carrier trans-port by doping of electrons into the conduction level of core–PbTe.[109] It also strongly localizes the holes within the PbTe core valence level and result in the enhanced n-type electrical conductivity.[109] Furthermore, the lattice mismatch between PbTe and PbS phases resulted in acoustic impedance mismatch which strongly reduced thermal conductivities of the core–shell composites. As a result, PbTe@PbS core–shell nanocomposites with a thermoelectric figure of merit ($zT \sim$ 1.1 at 710 K) much higher than the pure PbTe and PbS nanomaterials were obtained.[107] The changes in the electrical conductivity, Seebeck coefficient, thermal conductivity, and figure of merit along with the variation in the activation energy for electrical transport (E_a) as a function of the PbS concentration in $(PbTe)_{1-x}(PbS)_x$ nanocomposites are shown in Fig. 6(c).

The energy filtering effects have been observed by Ou et al. in all oxide $TiC_{1-x}O_x@TiO_y$–TiO_2 ($x < 1, 1 < y < 2$) core–shell nanostructures.[110] These core–shell heterostructures were synthesized with an anodization process assisted by the sol–gel chemical route as illustrated in Fig. 7. The shell layer made up of TiO_y–TiO_2 creates a double-barrier for the charge carriers, which scatters most of the low-energy carriers leading to enhancement of the Seebeck coefficient. This carrier filter mechanism is illu-strated in Fig. 7(b–e); in the $TiC_{1-x}O_x@TiO_y$–TiO_2 heterostruc-tures with the graded potential barrier, the first interfacial barrier between the $TiC_{1-x}O_x$ and TiO_y selectively scatters low-energy carriers. Further, the second interface TiO_2 barrier between the core ($TiC_{1-x}O_x$) and shell (TiO_y–TiO_2) scatters partial high-energy carriers. Consequently, carriers with higher energy can be able to pass through the double-barrier. In addition, the channel between the TiO_2 particles in these heterostructures can allow partial
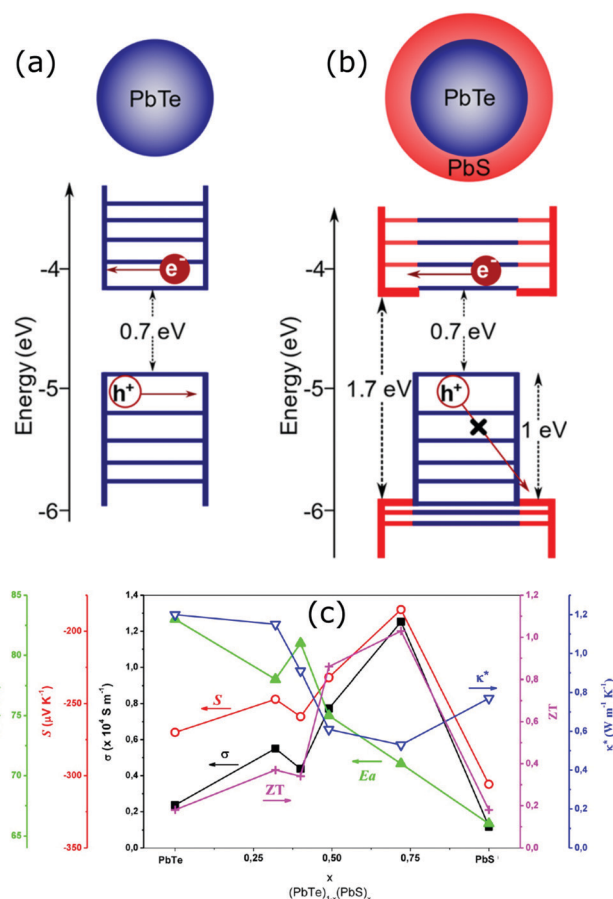

Fig. 6 Schematic energy diagrams of the (a) PbTe core nanocrystal and (b) PbTe@PbS core–shell nanocrystal. Reproduced with permission from ref. 109, (Copyright 2020 American Chemical Society). (c) is the variations in the electrical conductivity (σ), Seebeck coefficient (S), thermal conduc-tivity (κ^*), and figure of merit (zT) (at 710 K) along with the variation in the activation energy for electrical transport (E_a) as a function of the PbS concentration in $(PbTe)_{1-x}(PbS)_x$ nanocomposites. Reproduced with permission from ref. 107, Copyright 2013 American Chemical Society.

high-energy carriers to pass through, which helps maintain good electrical transport. Overall, these "all oxide" core–shell heterostructures have shown high Seebeck coefficients while maintaining a relatively good electrical conductivity in addition to the reduced thermal conductivity via possible double-barrier filtering effects due to engineered interfacial barriers as a result, a high zT up to 0.84 at 973 K has been observed.[110]

Similarly, enhanced Seebeck coefficient with reduced thermal conductivity was observed in $Au@Cu_2Se$ core–shell nano-particles.[111] Jin et al. synthesized these nanoparticles with differ-ent shell thicknesses through the hydrothermal route by control-ling the precursor concentration.[111] With the improvements in the Seebeck coefficient by energy filtering in the core–shell inter-face and reduced lattice thermal conductivity of core–shell due to coherent phonon scattering, a high zT value of 0.61 was obtained at 723 K in $Au@Cu_2Se$ core–shell nanoparticles with a shell thickness of 21 nm. The zT achieved from the core–shell structures is higher than that of the composite mixture of Au and Cu_2Se particles or pure Cu_2Se (Fig. 8). In a recent study, Sharma et al.
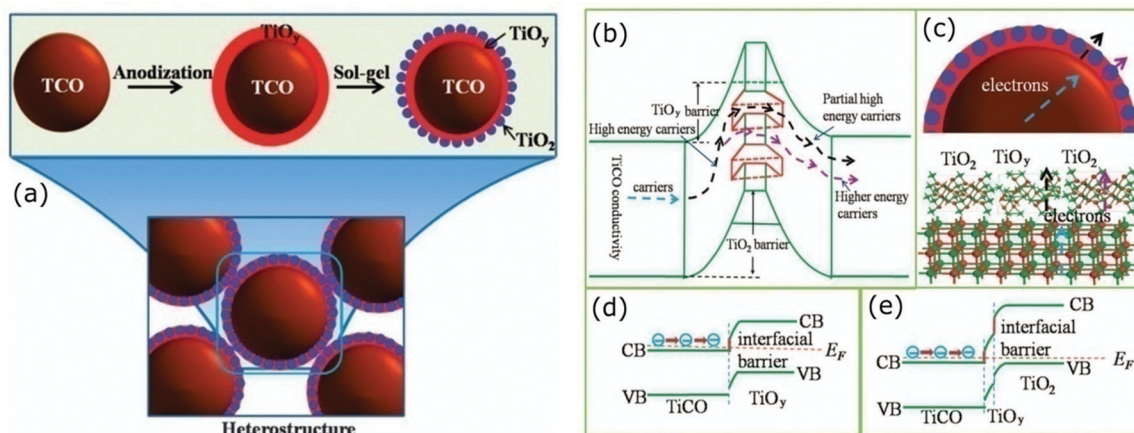
Fig. 7 (a) Schematic illustration of the formation of the $TiC_{1-x}O_x@TiO_y-TiO_2$ heterostructures *via* anodization process. The mechanism of carrier transport through the double-barrier: (b) carrier paths where the first interfacial TiO_y barrier selectively scatters low-energy carriers and the TiO_2 barrier further scatters partial high-energy carriers, (c) transport schemes of the carriers in the heterostructures and at the interface, (d) and (e) show the band diagrams of the all-oxide $TiC_{1-x}O_x@TiO_y$ and $TiC_{1-x}O_x@TiO_y-TiO_2$ heterostructured interfaces. Reproduced with permission from ref. 110, Copyright 2015 Nature Publishing Group.

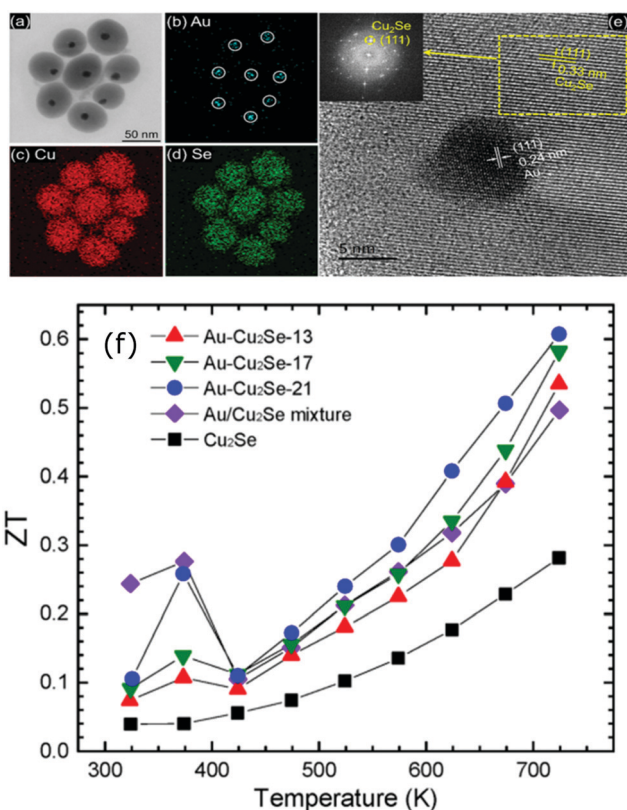**Fig. 8** (a) Transmission electron microscopes (TEM) images of $Au@Cu_2Se$ nanoparticles and the elemental mapping pictures of (b) Au, (c) Cu, (d) Se, (e) shows the high resolution-TEM images of a $Au@Cu_2Se$ nanoparticles (inset is the corresponding Fourier transform), and (f) shows the figure of merit (zT) of $Au@Cu_2Se$ core–shell nanocomposite samples of different shell thicknesses (21, 17, and 13 nm) along with pure Cu_2Se, Au/Cu_2Se mixture sample. Reproduced with permission from ref. 111, Copyright 2020 American Chemical Society.

reported an ultralow thermal conductivity in $Cu@Cu_2O$ core–shell nanocomposites synthesized using a facile solution-phase method

as illustrated in Fig. 9.[112] These core–shell samples have shown an ultralow thermal conductivity of about 10^{-3} of the bulk copper with a large Seebeck coefficient of ~ 373 μV K^{-1}, resulting in a zT of 0.16 at 320 K, showing their potential for low-cost thermoelectrics. In another interesting work by Ibáñez *et al.*, tunable p-type transport behaviour has been observed in Pb chalcogenides using alkali metal chalcogenides as capping ligands.[113] It is interesting to note that in these works, the surface functionalization with K^+ and Na^+ ions has resulted in core–shell type nanostructures which assisted in introducing controlled amounts of dopants.

Core–shell nanowires have also attracted tremendous interest due to their remarkable electronic and thermal properties.[114] Several experimental and theoretical studies have shown the possibilities of producing promising thermoelectric materials in the form of core–shell nanowires.[115–118] Successful examples include Ge@Si,[114,115,119,120] Si@Ge,[121,122] GaAs@AlAs,[117] GaAs@AlGaAs,[123] Bi_2S_3@Bi,[116] Bi@Te,[124] Te@Bi,[125] Bi@TiO_2,[126] multiwalled carbon nanotubes $(MWCNT)@Sb_2Te_3$,[127] Bi_2Te_3@MWCNT,[128] and so on. These special heterostructures show superior electronic properties and a significant reduction in thermal conductivity compared to single element nanowires. The radial heterostructure core–shell nanowires show remarkable carrier mobility due to the band offsets.[119] For example, high hole mobility of 730 cm^2 V^{-1} s^{-1} was observed in Ge@Si nanowire heterostructures based field-effect transistors (NWFET), which is ten times high compared to the Si p-MOSFET (metal–oxide–semiconductor field-effect transistors).[129] It is also more than twice that of Ge or SiGe PMOS (p-channel metal–oxide–semiconductor) devices.[129]

Hu *et al.* reported nonequilibrium molecular dynamics simulations on the effect of Ge coatings on the thermal properties of Si nanowires.[122] Their results show that a simple Ge shell coating of thickness 1 or 2 unit cells on single crystalline Si nanowires can lead to a dramatic decrease (by 75%) in thermal conductivity compared to uncoated Si nanowires. They found that such a dramatic fall in thermal conductivity in core–shell
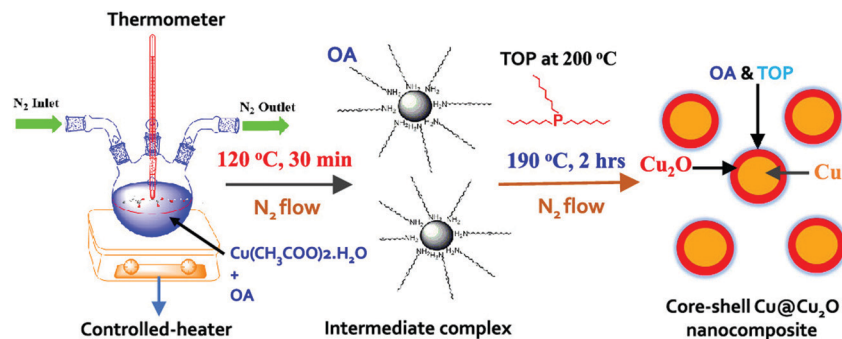
Fig. 9 Schematic of the synthesis process of Cu@Cu$_2$O core–shell nanoparticles using copper acetate hydrate, oleylamine (OA), and trioctylphosphine (TOP). Reproduced with permission from ref. 112, Copyright 2020 American Chemical Society.

nanowire comes from the reduction and localization of long-wavelength phonon modes at the core–shell interface and also from high-frequency non-propagating diffusive modes. To support this, they systematically studied the changes in the vibrational density of states (VDOS) of surface Si atoms on the nanowire after the addition of the Ge shell coating. The results of VDOS shown in Fig. 10(a) indicate that there are no notable changes in the VDOS for Si atoms in the centre of the nanowires core. In contrast, significant depression of the low-frequency part is (below 6 THz) and also at the high-frequency part (between 16–17 THz) can be observed for core–shell nanowires as compared to pure Si nanowires (Fig. 10(b)). Such depressions can originate from a lattice mismatch and atomic mass differences.[122] This also appears to be true for Si coated Ge or Ge@Si core–shell nanowires, which is evident from Wingert *et al.*'s work,[118] who studied thermal properties of Ge@Si. Their results show the reduction in thermal conductivity with observed values in the range of 1.1–2.6 W m^{-1} K^{-1} at around 108–388 K, which is lower than Ge nanowires and also even lower than that of SiGe alloy nanowires.[118] These studies and the observed improvements with such structures indicate that the core–shell structures can be more promising than alloys or composite materials.

Similar thermal conductivity reduction has also been reported for Bi@Te nanowires. In addition, a recent study by Kang *et al.* suggests that with rough interfaces between the core and shell materials, a further reduction can be achieved.[124] A comparison of thermal conductivities between smooth and rough interface based Bi@Te core–shell nanowires is shown in Fig. 11. Bi$_2$Te$_3$ is an excellent and commercially used thermoelectric material. However, the expensive, highly scarce, and toxic nature of tellurium is a matter of concern for extending the thermoelectric generator applications.[130,131] Replacing tellurium with sulfur, an abundant and cheap element can be a promising strategy. This idea encouraged many researchers to find sulfur and selenide based metal chalcogenides for thermoelectric applications.[132,133] For illustration, Bi$_2$S$_3$ is an n-type semiconductor with a very high Seebeck coefficient and low thermal conductivity can be a replacement for Bi$_2$Te$_3$, but it suffers from its poor electrical conductivity.[134] A recent work on Bi$_2$S$_3$@Bi core–shell nanowires demonstrated that the electrical conductivity of the Bi$_2$S$_3$ can be enhanced significantly with Bi shell

coating on Bi$_2$S$_3$ nanowires.[116] These Bi$_2$S$_3$@Bi core–shell nanowires were obtained from treating Bi$_2$S$_3$ nanowires in a hydrazine solution by a hydrothermal method. Three orders of magnitude greater electrical conductivity was observed from Bi$_2$S$_3$@Bi core–shell nanowires sample than that of a pristine Bi$_2$S$_3$ sample, which resulted in a good zT of 0.36 at 623 K.

Due to the low-cost, lightweight, and interesting electrical properties of carbon nanotubes (CNTs), they have been widely studied for energy-related applications.[135–138] CNTs are special one-dimensional materials with high carrier mobilities, high thermal conduction, high strength, and so on.[139,140] They have also shown promising thermoelectric properties when they are modified or treated with organic molecules/polymer compounds, impurity atoms, *etc.*[141–145] Similarly, the effects of core–shell structures on thermoelectric performance of CNTs have also been reported.[139,146] For instance, Chiang *et al.* reported a scalable two-step reaction route to fabricate C@BCN core–shell nanotubes in bulk quantities.[146] The CNTs were dissolved in an SDS (sodium dodecyl sulfate) aqueous solution to form dispersion and then B$_2$O$_3$ powder was added to the CNT/SDS dispersion. The final reaction was carried out at high temperatures to obtain C@BCN core–shell nanotubes, as illustrated in Fig. 12. The thin-films based on these C@BCN core–shell nanotubes have shown an improved Seebeck coefficient, which led to a 6.4-fold increase in the power factor. Similar thermoelectric enhancements were also observed from *in situ* polymerisation of PEDOT on graphene platelets, coral-like PEDOT/single-walled carbon nanotubes (SWCNT), polypyrrole (PPy)/graphene core–shell type thermoelectric compounds.[147–152]

3.2. Core–shell nanostructures in bulk semiconductors

Thermoelectric properties of the bulk semiconductors have been routinely modified with traditional impurity doping processes, where the ionized impurities are used to modify the electronic properties of the host bulk.[153–155] With the advancement in material fabrication, doping bulk materials with nano-inclusions has been becoming one of the most effective strategies to improve thermoelectric properties.[156–159] Researchers have further found promising results when the bulk semiconductors are doped with core–shell nanoparticles.[52] The use of core–shell nanoparticles embedded in bulk semiconductors can lead to a very high thermoelectric
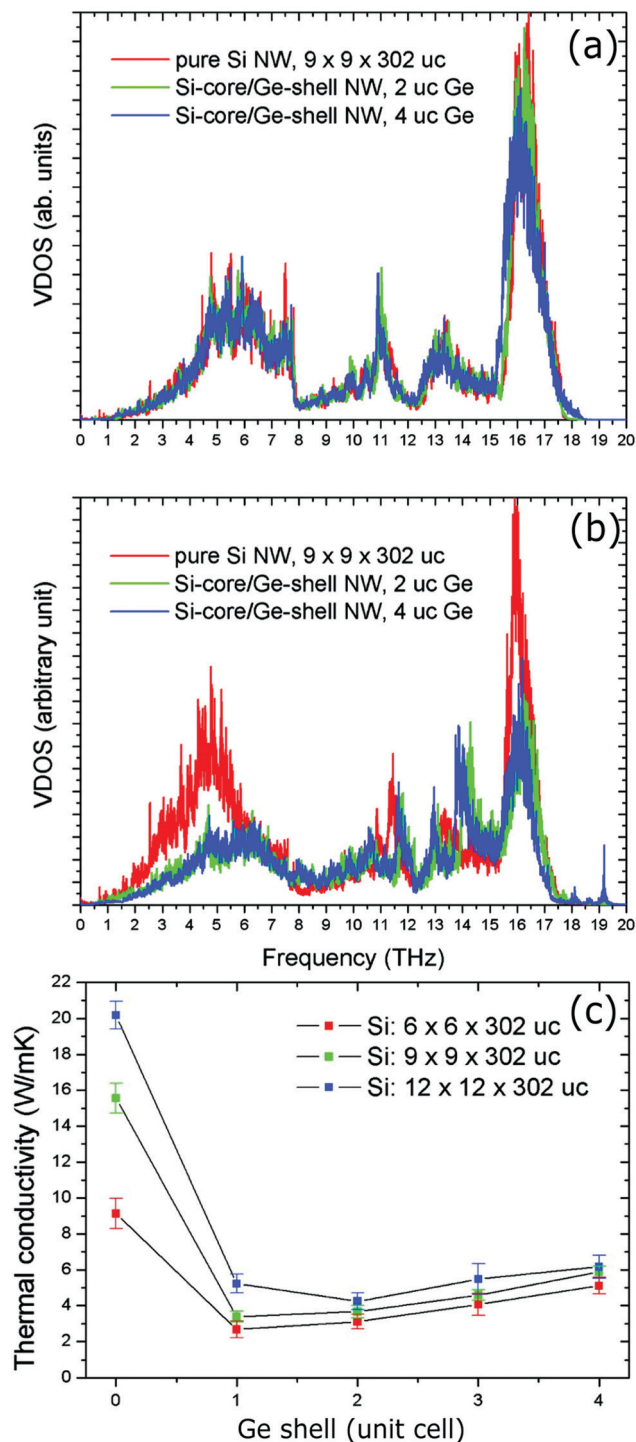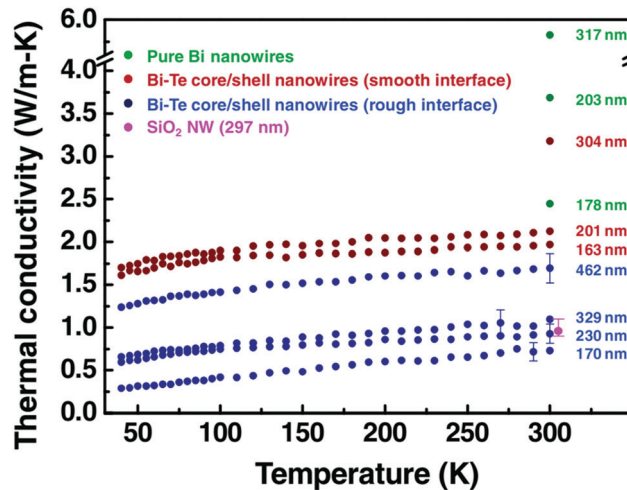
Fig. 11 The thermal conductivity data of pure Bi nanowires, the rough interface Bi@Te core–shell nanowires with diameter 170, 230, 329, and 462 nm, and the smooth interface Bi@Te core–shell nanowires with diameter 163, 201, and 304 nm. The graph also shows the thermal conductivity of SiO$_2$ nanowire (at 300 K) to confirm the reliability of the measurement. Reproduced with permission from ref. 124, Copyright 2011 Wiley-VCH.
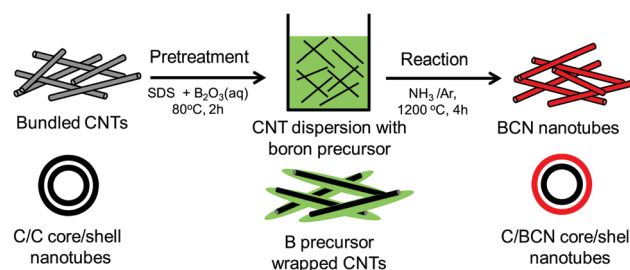

Fig. 12 Schematic process of two-step reaction route to prepare C@BCN core–shell nanotubes. Reproduced with permission from ref. 146, Copyright 2016 Elsevier B.V.

Fig. 10 (a) Vibrational density of states (VDOS) of Si atoms at the center of the Si core. (b) VDOS of Si atoms located at the Si–Ge interface (uc: unit cell). (c) Thermal conductivity of the Si@Ge nanowire as a function of the number of Ge shell layers and for different cross-sectional areas of the Si core. Reproduced with permission from ref. 122, Copyright 2011 American Chemical Society.

power factor. Particularly, when embedded core–shell nanoparticles have resonant levels falling within the energy band of the host bulk semiconductor, they can significantly enhance

the power factor over the bulk.[52] This study also predicted a more than 80% enhancement in the thermoelectric power factor in PbTe at low temperatures.[52]

An experimental study that demonstrates the effect of embedded core–shell particles inside the bulk is reported by Li et al.[160] In this work, the added Zn$_4$Sb$_3$ into SnTe converted into Sb@ZnTe core–shell microstructures in the matrix of SnTe due to sequential in situ reactions between the Zn$_4$Sb$_3$ additive and SnTe matrix, as schematically illustrated in Fig. 13.[160] The resulting compound exhibited an ultralow lattice thermal conductivity of 0.48 W m^{-1} K^{-1}. In addition, the electrical properties were also improved with reaching a maximum zT of 1.32 at 873 K, which was about 220% more than the pristine SnTe. In a similar approach, Ma et al. observed the formation of SnO$_2$ layers around the BiCuSeO nanoinclusions doped into SnTe during a high temperature solid state reaction, which resulted in the SnTe compound with BiCuSeO@SnO$_2$ core–shell nanoinclusions.[100] They observed a high zT of 1.21 at 835 K for a 5% BiCuSeO doped sample, which was 190% improvement
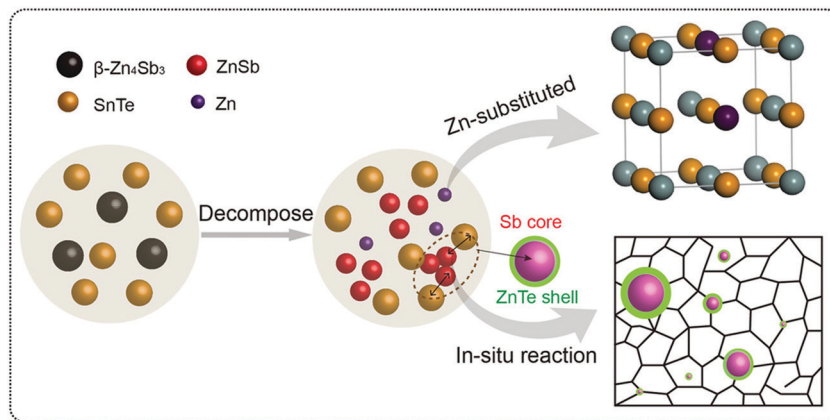
Fig. 13 The schematic illustration of the reaction process that forms embedded core–shell structures. Reproduced with permission from ref. 160, Copyright 2020 Wiley-VCH.

over SnTe. Also, Yaprintsev *et al.* found enhanced thermo-electric efficiency, where zT of a bulk Bi_2Te_3 compound was improved from $zT = 0.3$ to $zT = 0.67$ (at 400 K) by introducing Ni@NiTe$_2$ core–shell inclusions into Bi_2Te_3 matrix.[161] Similarly, Cai *et al.* found improved thermoelectric performance from PbSe after the incorporation of core–shell nanoscale CdSe precipitates in PbSe.[162] As shown by Fig. 14, the CdSe nano-precipitates in the PbSe exhibit a zinc blende crystal structure covered with a thin wurtzite layer at the matrix interface, forming an embedded core–shell structure in PbSe. These tetrahedral shaped nano-precipitates with significant local strains cause a reduction in lattice thermal conductivity of the compound and help achieve better thermoelectric performance.

In recent work, Xiang *et al.* reported a facile route to construct locally nanostructured PbTe in a micro-sized PbTe frame.[163] They mixed PbTe@C:Ag nanoparticles and PbTe nanocubes through spark plasma sintering (SPS) producing PbTe/PbTe@C:Ag type structure as shown in Fig. 15. Here, the carbon shell on PbTe acts as a barrier that prevents the growth of the grains and helps to form locally nanostructured PbTe regions with a lot of grain boundaries and interfaces. In addition, Ag atoms may work as dynamic dopants and can enhance the high-frequency phonon scattering and suppress the bipolar effect. The resulting compound has shown a low lattice thermal conductivity of 0.39 W m^{-1} K^{-1} and a high power factor of 20.4 μW cm^{-1} K^{-2} with a high zT of 1.65 at 723 K.

Similarly, by introducing PbTe@C core–shell nanostructures into $Sn_{1-y}Sb_yTe$, Zhang *et al.* observed enhanced thermoelectric properties.[164] These unique hierarchical structures possess an ultralow lattice thermal conductivity of ∼0.48 W m^{-1} K^{-1} almost approaching amorphous limits (∼0.40 W m^{-1} K^{-1}). These compounds have shown a maximum figure of merit (zT) of 1.07 at 873 K, which is approximately ∼155% higher than that of pure SnTe.[164] They also found that the PbTe@C core–shell structures exhibit great thermal stability upon repeated measurements, indicating promising for practical applications. Zhang *et al.* compared the effects of adding Bi_2S_3 and Bi_2S_3@Bi core–shell nanorods into the $Cu_{1.8}S$ bulk.[165] They found that the enhancement in zT achieved from incorporating Bi_2S_3@Bi

Fig. 14 Scanning and transmission electron microscopy (S/TEM) images of PbSe-CdSe sample. (a) High-angle annular dark field image showing the embedded triangular nano-precipitates in the matrix. (b) Energy-dispersive X-ray spectroscopy (EDS) mapping. (c) TEM image showing a core–shell precipitate in the matrix. (d) Selected area diffraction (SAED) pattern taken along the [110] zone axis, which reveals the interface is the wurtzite CdSe phase. (e) High-resolution STEM image with a HAADF mode image showing the core–shell sections of CdSe with PbSe matrix. (f–i) Show the atomic stacking of the matrix, interface between the matrix and shell, the shell, and core of the precipitate. Reproduced with permission from ref. 162, Copyright 2020 Royal Society of Chemistry.
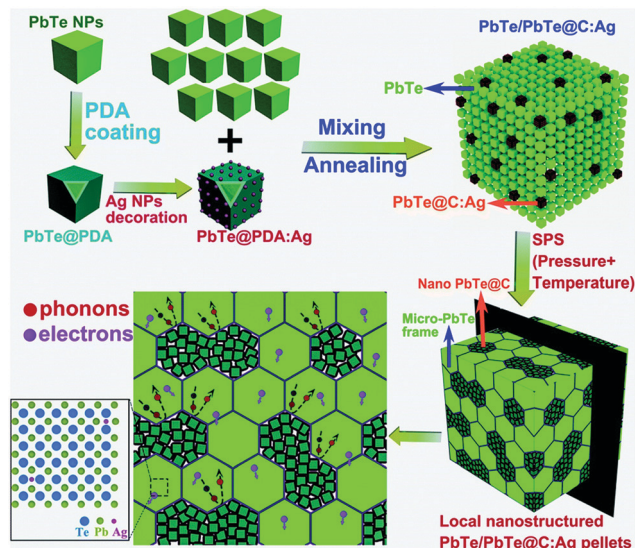
Fig. 15 Schematic illustration showing the formation of the locally nano-structured PbTe/PbTe@C:Ag. The polydopamine (PDA) derived thin carbon shell prevents the grain growth. The transport of electrons and phonons through the hierarchical structures of the compound is also illustrated. Reproduced with permission from ref. 163, Copyright 2019 Royal Society of Chemistry.

core–shell particles was better than adding Bi_2S_3. A maximum zT of 0.77 (which is 2.4 times higher than that of the pure $Cu_{1.8}S$) was observed (at 723 K) from 3 wt% Bi_2S_3@Bi core–shell particles introduced sample while it was 0.62 for 3 wt% Bi_2S_3 added sample. Similarly, an enhanced zT of 1.2 (at 450 K) was obtained from a composite constructed from Bi_2Te_3 nanoparticles and Bi_2S_3@Bi nanowires.[166] Thermoelectric enhancements in these composites are mainly attributed to the presence of a hierarchical network-like structure formations due to core–shell configurations.

3.3. Secondary phase at grain boundaries

Grain boundary engineering has been an important and promising approach in thermoelectrics.[167,168] It has significant effects on the reduction of thermal conductivity in bulk nanostructured thermoelectric materials. Interestingly, a secondary phase formed at the grain boundaries of the host matrix can act like core–shell like structures and enhance the thermoelectric performance of the resulting materials. Several studies have found such special structures are beneficial and the electrical and thermal properties of the host materials can be easily modified in order to make them suitable for thermoelectric applications. Most of the reported works on this type of core–shell structure are based on graphene/inorganic hybrid compounds.[42,168–172] The layer-like structure of graphene effectively coats on the particles/grains of the inorganic host material and forms carbon encapsulated grains. Due to their special electrical, optical, and thermal properties, graphene added composite materials have been extensively studied for different energy conversion and sensing applications.[173–182] A simple schematic illustration on the formation of graphene covered
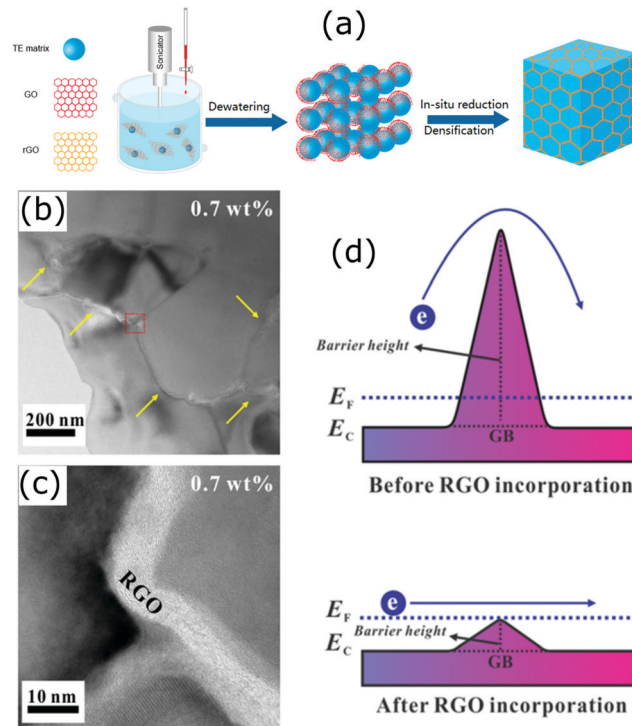

Fig. 16 (a) Schematic illustration of the synthesis of a bulk composite containing graphene (RGO) layer encapsulated grains (Reproduced with permission from ref. 183, Copyright 2020 American Chemical Society). (b and c) HRTEM micrographs of the STO−0.7 wt% RGO composite. (d) Schematic of double Schottky barrier of the STO–RGO composites. Reproduced with permission from ref. 171, Copyright 2019 Nature Publishing Group.

grains in the bulk is shown in Fig. 16.[183] The illustrated process involves the mixing of graphene oxide layers with inorganic thermoelectric matrix (TE matrix) and then *in situ* reduction of the resulting material to obtain graphene or reduced graphene oxide (RGO) encapsulated inorganic grains/particles. Several composites with such structures were successfully developed by Zong *et al.* with improved thermoelectric performances.[168,169] As the addition of graphene into the bulk introduces enormous interfaces, the interfacial phonon scattering will be enhanced and therefore the lattice thermal conductivity of the compound is expected to decrease. For example, depression in thermal conductivity has been observed in the skutterudite compounds with graphene-modified grain-boundary complexion.[168] Encapsulating even micron-sized skutterudite (n-type $Yb_yCo_4Sb_{12}$) grains with graphene resulted in a significantly reduced thermal conductivity with a high zT of 1.5 (at 850 K), and similarly, a zT of 1.06 (at 700 K) was achieved in p-type $Ce_yFe_3CoSb_{12}$.[168]

In many polycrystalline compounds, their thermoelectric performance is greatly restricted due to the resistive grain boundaries, which are also known as the double Schottky barriers (DSB).[184] It is supposed that the electrons trap at the grain boundaries and do not involve in the electrical conduction, and also act as scattering centres.[171] Therefore, breaking or reducing the DSB effect is important to make such compounds useful for thermoelectric applications. A number of studies
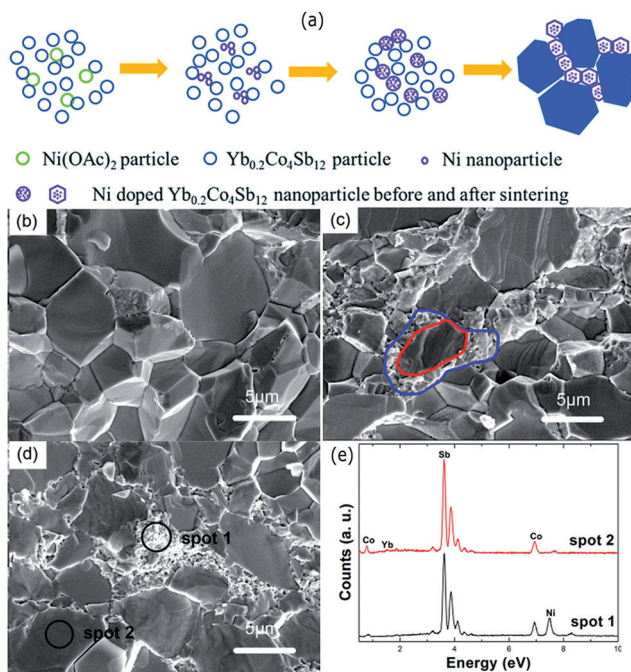
Fig. 17 (a) Schematic of the Ni-rich shells formation at the grain boundaries. The thermal decomposition of nickel acetate formed Ni nanoparticles during the process. The large blue polygons represent the grains of the $Yb_{0.2}Co_4Sb_{12}$. SEM images of the pure $Yb_{0.2}Co_4Sb_{12}$ (b) and (c and d) are the Ni doped samples with 0.2 wt% and 0.5 wt%, respectively. (e) EDS spectrum of spots 1 and 2 marked in (d). Reproduced with permission from ref. 189, Copyright 2015 Royal Society of Chemistry.

have found that it can be done *via* grain boundary engineering.[171,184,185] In an interesting work by Rahman *et al.*, they found that the incorporation of reduced graphene oxide into strontium titanium oxide (STO) weakens the DSB (Fig. 16(d)).[171] This has led to a simultaneous increase in the carrier concentration and carrier mobility of the STO.

Chen *et al.* reported a scalable wet chemical method to fabricate $Cu_{2-x}S$ particles encapsulated in a thin carbon shell that forms $Cu_{2-x}S@C$ core–shell composites.[42] The electrical conductivity of the $Cu_{2-x}S@C$ core–shell composite has seen a 50% increase compared to that of the pure uncoated $Cu_{2-x}S$ compound. The resulting core–shell composite possessed an ultra-low lattice thermal conductivity of 0.22 W m^{-1} K^{-1} and a maximum zT of 1.04 at 773 K. These improvements are attributed to an increase in the carrier concentration and enhanced phonon scattering at the interfaces formed due to graphene layers. Similarly, Tang *et al.* fabricated graphene encapsulated on $Cu_{2-x}S$ grains with mechanical alloying (MA) and spark plasma sintering (SPS) processes.[186] Here also, a high power factor of 1197 μW m^{-1} K^{-2} and a significant enhancement in zT were observed with the highest zT of 1.56 at 873 K. Furthermore, generally, copper sulfides show Cu$^+$ superionic behaviour at higher temperatures.[187,188] Here, the presence of the 3D interface network of graphene layers restricts the superionic behaviour of Cu$^+$ ions, which improved the thermal stability of the compound.

Modification of grain boundaries to achieve energy filtering effects has also been carried out with other compounds. Fu *et al.* modified the grains of Yb filled skutterudites with Ni to obtain "core–shell" structure.[189] Such core–shell structure was obtained due to the thermal diffusion of well-dispersed Ni nanoparticles in the skutterudite ($Yb_{0.2}Co_4Sb_{12}$) powder compound through a hot pressing process. The resulting compound was composed of the skutterudite core grains surrounded by Ni-rich skutterudite nanograin layers, as shown in Fig. 17. The electrical conductivity of the compound was greatly enhanced due to the presence of Ni-rich grains, which was responsible for the increased carrier concentration as well as carrier mobility. The thermoelectric power factor was found to increase after the incorporation of Ni nanoparticles along with the reduction in lattice thermal conductivity due to extra phonon scattering from core–shell structures. As a result, the Ni added compounds have shown a maximum zT of 1.07 at 723 K.

Kim *et al.* coated extremely thin ZnO layers on the $Bi_{0.4}Sb_{1.6}Te_3$ (BST) powders *via* an atomic layer deposition (ALD) technique.[190] Compounds with numerous heterogeneous interfaces were created by this strategy with the formation of BST@ZnO core–shell structures. The results of this study

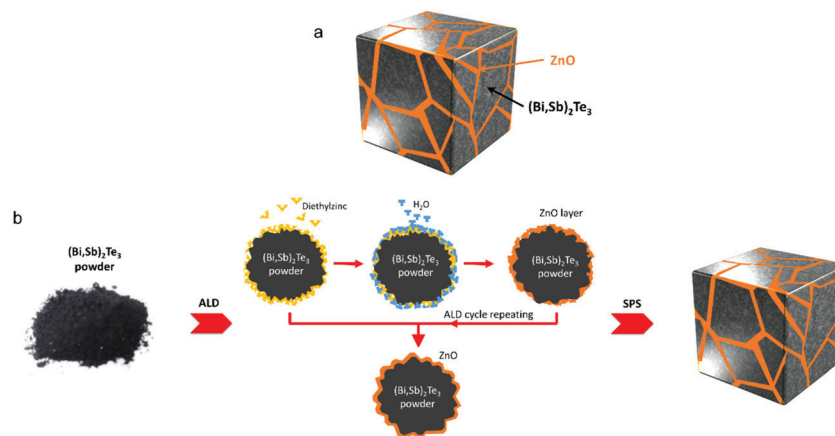Fig. 18 (a) Schematic structure of BST@ZnO composite composed of ZnO coated BST ($Bi_{0.4}Sb_{1.6}Te_3$) grains. (b) Schematic fabrication process for BST@ZnO core–shell structures. Reproduced with permission from ref. 190, Copyright 2019 American Chemical Society.

Table 1 Details of enhanced thermoelectric figure of merits (zT values) discussed in this review

Material	zT observed	zT enhancement (approx.)	Ref.
PbTe@PbS core–shell nanocomposites	1.1 at 710 K	6 times of the PbS or PbTe	Ibáñez et al.[107]
TiC$_{1-x}$O$_x$@TiO$_y$–TiO$_2$ core–shell nanocomposites	0.84 at 973 K	—	Ou et al.[110]
Au@Cu$_2$Se core–shell nanocomposites	0.61 at 723 K	2 times of the Cu$_2$Se	Jin et al.[111]
Cu@Cu$_2$O core–shell nanocomposites	0.16 at 320 K	—	Sharma et al.[112]
Bi$_2$S$_3$@Bi core–shell nanowires composites	0.36 at 623 K	2 times of the Bi$_2$S$_3$	Ge et al.[116]
Sb@ZnTe core–shell structures in SnTe	1.32 at 873 K	3 times of the SnTe	Li et al.[160]
BiCuSeO@SnO$_2$ core–shell nanoinclusions in SnTe	1.21 at 835 K	3 times of the SnTe	Ma et al.[100]
Ni@NiTe$_2$ core–shell inclusions in Bi$_2$Te$_3$ matrix	0.67 at 400 K	2 times of the Bi$_2$Te$_3$	Yaprintsev et al.[161]
PbTe/PbTe@C:Ag composites	1.65 at 723 K	8 times of the PbTe	Xiang et al.[163]
PbTe@C core–shell nanostructures in Sn$_{1-y}$Sb$_y$Te	1.07 at 873 K	2.5 times the SnTe	Zhang et al.[164]
Bi$_2$S$_3$@Bi core–shell nanorods in the Cu$_{1.8}$S	0.77 at 723 K	2.5 times of the Cu$_{1.8}$S	Zhang et al.[165]
Composite of Bi$_2$Te$_3$ nanoparticles and Bi$_2$S$_3$@Bi nanowire	1.2 at 450 K	—	Zhang et al.[166]
Graphene encapsulated Yb$_y$Co$_4$Sb$_{12}$	1.5 at 850 K	—	Zong et al.[168]
Graphene encapsulated p-type Ce$_y$Fe$_3$CoSb$_{12}$	1.06 at 700 K	—	Zong et al.[168]
Carbon encapsulated Cu$_{2-x}$S composites	1.04 at 773 K	1.2 times of the Cu$_{2-x}$S	Chen et al.[42]
Reduced graphene oxide on strontium titanium oxide (STO) grains	0.05 at 700 K	2.5 times of the STO	Rahman et al.[171]
Graphene encapsulated Cu$_{2-x}$S composites	1.56 at 873 K	—	Tang et al.[186]
Composites of Yb filled skutterudite (Yb$_{0.2}$Co$_4$Sb$_{12}$)@Ni-rich skutterudite	1.07 at 723 K	2 times of the Yb$_{0.2}$Co$_4$Sb$_{12}$	Fu et al.[189]
ZnO coated Bi$_{0.4}$Sb$_{1.6}$Te$_3$ grains	1.50 at 360 K	1.5 times of the Bi$_{0.4}$Sb$_{1.6}$Te$_3$	Kim et al.[190]
CdTe coated SnTe grains	1.90 at 929 K	—	Hwang et al.[191]
Composite of Cu$_2$Se coated CNTs	2.40 at 1000 K	—	Nunna et al.[139]

demonstrated that the incorporation of ZnO thin layers into the BST matrix can block phonons and also help tune carrier density from impurity doping at the grain boundaries. An optimised thickness of ZnO coating resulted in a high thermoelectric zT of 1.50 (at 329–360 K). Such a high zT at around room temperature in addition to the simplicity of the fabrication process (illustrated in Fig. 18) indicate that the approach can be very useful to make mass production of core–shell type composites. In a similar approach, Hwang et al. observed thermal conductivity reduction in SnTe/CdTe nanocomposites composed of CdTe coated layers on the surface of SnTe grains.[191] They found that the acoustic impedance mismatch between the coated CdTe layers and the SnTe grains resulting in a low thermal conductivity of 1.16 W m^{-1} K^{-1} and as a result, a high zT of 1.90 was observed at 929 K. Similarly, composite materials with well distributed CNTs at the molecular level can also modify grain boundaries of the host matrix. For instance, Nunna et al. observed an *in situ* growth of Cu$_2$Se on the surface of CNTs during the fabrication of Cu$_2$Se/CNT hybrid composites.[139] The resulting composites have shown a record-high zT of 2.4 at 1000 K. The enhanced thermoelectric figure of merits (zT values) discussed in this review are summarized in Table 1. These enhancements have been achieved either directly from intentionally formed core–shell structures or from inadvertently formed core–shell structures during the fabrication, both of which have induced multiple barriers that improved the filtering effects alongside reduced thermal conductivity and resulted in materials with enhanced thermoelectric performance.

4. Conclusion and prospects

The energy filtering effect observed from core–shell structures is a recent promising strategy to enhance materials' thermoelectric properties.[192] It is evident from the research works discussed in this review, where many theoretical predictions and

experimental works have proved that core–shell nanostructures can lead to materials with remarkable thermoelectric properties.

It is worth noting that the overall enhancement of thermoelectric performance requires optimization of several parameters which are strongly interrelated, such as the number of carriers, carrier mobility, phonons, and their coupling effects.[12,193] In addition, based on thermoelectric results reported in the literature, in many cases it is true that the energy filtering effect is not a sole factor to improve materials performance.[194] Several other factors such as mechanisms of electron and phonon transport in different conditions, crystal structures, chemical compositions, grain orientations, nano/microstructures, etc. also play their roles.[194] Also, it is important to note that the reduction of effective mass after the reduced carrier concentration due to energy filtering effects can be detrimental to the increase of the Seebeck coefficient. Therefore, overall improvements in the thermoelectric performance requires a compromise between all the electrical and thermal parameters. Thermal stability of the core–shell materials is also an important and essential requirement when these are to be used for practical applications. The core–shell structures should be thermally stable with respect to their phase or physical structure as well as chemical composition in order to implement them for real applications. Prior knowledge and understanding of the band structures of the materials chosen to fabricate core–shell nanostructures and the resulting band bending/band offsets are essential to decide their suitability and optimize the thermoelectric performance. Overall, the energy filtering effects can provide new opportunities to modify the electron and phonon transport through core–shell structural engineering.

Author contributions

Rafiq Mulla: writing – original draft, conceptualization, data collection, formal analysis. Charles W. Dunnill: supervision, resources, funding acquisition.

Conflicts of interest

There are no conflicts to declare.

Acknowledgements

References

1 M. S. Dresselhaus, G. Chen, M. Y. Tang, R. G. Yang, H. Lee, D. Z. Wang, Z. F. Ren, J. P. Fleurial and P. Gogna, *Adv. Mater.*, 2007, **19**, 1043–1053.

2 L. E. Bell, *Science*, 2008, **321**, 1457–1461.

3 W. Wu, G.-K. Ren, X. Chen, Y. Liu, Z. Zhou, J. Song, Y. Shi, J.-M. Jiang and Y.-H. Lin, *J. Mater. Chem. A*, 2021, **9**, 3209–3230.

4 L. Yang, Z.-G. Chen, M. S. Dargusch and J. Zou, *Adv. Energy Mater.*, 2018, **8**, 1701797.

5 R. Phillips, W. J. F. Gannon and C. W. Dunnill, Alkaline Electrolysers, in *Electrochemical Methods for Hydrogen Production*, Royal Society of Chemistry, 2019.

6 R. Phillips and C. W. Dunnill, *RSC Adv.*, 2016, **6**, 100643–100651.

7 R. Mulla and C. W. Dunnill, *ChemSusChem*, 2019, **12**, 3882–3895.

8 X. Zhang, W. Gao, X. Su, F. Wang, B. Liu, J.-J. Wang, H. Liu and Y. Sang, *Nano Energy*, 2018, **48**, 481–488.

9 S.-M. Shin, J.-Y. Jung, M.-J. Park, J.-W. Song and J.-H. Lee, *J. Power Sources*, 2015, **279**, 151–156.

10 Y. Jia, Q. Jiang, H. Sun, P. Liu, D. Hu, Y. Pei, W. Liu, X. Crispin, S. Fabiano, Y. Ma and Y. Cao, *Adv. Mater.*, 2021, **n/a**, 2102990.

11 R. Mulla, D. R. Jones and C. W. Dunnill, *Adv. Mater. Technol.*, 2020, **5**, 2000227.

12 Y. Ouyang, Z. Zhang, D. Li, J. Chen and G. Zhang, *Ann. Phys.*, 2019, **531**, 1800437.

13 Y. Zhang, J.-H. Bahk, J. Lee, C. S. Birkel, M. L. Snedaker, D. Liu, H. Zeng, M. Moskovits, A. Shakouri and G. D. Stucky, *Adv. Mater.*, 2014, **26**, 2755–2761.

14 H. Mun, S.-M. Choi, K. H. Lee and S. W. Kim, *ChemSusChem*, 2015, **8**, 2312–2326.

15 A. J. Minnich, M. S. Dresselhaus, Z. F. Ren and G. Chen, *Energy Environ. Sci.*, 2009, **2**, 466–479.

16 P. Priyadarshi, A. Sharma, S. Mukherjee and B. Muralidharan, *J. Phys. D: Appl. Phys.*, 2018, **51**, 185301.

17 P. Priyadarshi and B. Muralidharan, *J. Phys. D: Appl. Phys.*, 2020, **54**, 095301.

18 R. K. Biswas and S. K. Pati, *ACS Appl. Energy Mater.*, 2021, **4**, 2081–2090.

19 S. Chandra, A. Banik and K. Biswas, *ACS Energy Lett.*, 2018, **3**, 1153–1158.

20 R. Abinaya, S. Harish, S. Ponnusamy, M. Shimomura, M. Navaneethan and J. Archana, *Chem. Eng. J.*, 2021, **416**, 128484.

21 C. Bauer, I. Veremchuk, C. Kunze, A. Benad, V. M. Dzhagan, D. Haubold, D. Pohl, G. Schierning, K. Nielsch, V. Lesnyak and A. Eychmüller, *Small Science*, 2021, **1**, 2000021.

22 R. Chen, J. Lee, W. Lee and D. Li, *Chem. Rev.*, 2019, **119**, 9260–9302.

23 S. Elyamny, E. Dimaggio, S. Magagna, D. Narducci and G. Pennelli, *Nano Lett.*, 2020, **20**, 4748–4753.

24 L. Yang, D. Huh, R. Ning, V. Rapp, Y. Zeng, Y. Liu, S. Ju, Y. Tao, Y. Jiang, J. Beak, J. Leem, S. Kaur, H. Lee, X. Zheng and R. S. Prasher, *Nat. Commun.*, 2021, **12**, 3926.

25 X. Jiang, C. Ban, L. Li, C. Wang, W. Chen and X. Liu, *AIP Adv.*, 2021, **11**, 055120.

26 Y. Xiong, G. Zhou, N.-C. Lai, X. Wang, Y.-C. Lu, O. V. Prezhdo and D. Xu, *ACS Nano*, 2021, **15**, 2791–2799.

27 X.-L. Zhu, P.-F. Liu, J. Zhang, P. Zhang, W.-X. Zhou, G. Xie and B.-T. Wang, *Nanoscale*, 2019, **11**, 19923–19932.

28 S. S. Kubakaddi, *J. Phys.: Condens. Matter*, 2021, **33**, 245704.

29 N. S. Sankeshwar, S. S. Kubakaddi and B. G. Mulimani, in *Advances in Graphene Science*, ed. M. Aliofkhazraei, IntechOpen, 2013, DOI: 10.5772/56720.

30 Y. Zhang, Y. Liu, M. Calcabrini, C. Xing, X. Han, J. Arbiol, D. Cadavid, M. Ibáñez and A. Cabot, *J. Mater. Chem. C*, 2020, **8**, 14092–14099.

31 M. Ibáñez, Z. Luo, A. Genç, L. Piveteau, S. Ortega, D. Cadavid, O. Dobrozhan, Y. Liu, M. Nachtegaal, M. Zebarjadi, J. Arbiol, M. V. Kovalenko and A. Cabot, *Nat. Commun.*, 2016, **7**, 10766.

32 W.-X. Zhou and K.-Q. Chen, *Sci. Rep.*, 2014, **4**, 7150.

33 M. F. Sanad, A. E. Shalan, S. O. Abdellatif, E. S. A. Serea, M. S. Adly and M. A. Ahsan, *Top. Curr. Chem.*, 2020, **378**, 48.

34 S. Wang, W. Xie, H. Li and X. Tang, *J. Phys. D: Appl. Phys.*, 2010, **43**, 335404.

35 Y. Xiao and L.-D. Zhao, *npj Quantum Mater.*, 2018, **3**, 55.

36 J. Sun, X. Su, Y. Yan, W. Liu, G. Tan and X. Tang, *ACS Appl. Energy Mater.*, 2020, **3**, 2–8.

37 M. R. Burton, T. Liu, J. McGettrick, S. Mehraban, J. Baker, A. Pockett, T. Watson, O. Fenwick and M. J. Carnie, *Adv. Mater.*, 2018, **30**, 1801357.

38 C. Chang, M. Wu, D. He, Y. Pei, C.-F. Wu, X. Wu, H. Yu, F. Zhu, K. Wang, Y. Chen, L. Huang, J.-F. Li, J. He and L.-D. Zhao, *Science*, 2018, **360**, 778.

39 S. Chandra and K. Biswas, *J. Am. Chem. Soc.*, 2019, **141**, 6141–6145.

40 R. Basu, S. Bhattacharya, R. Bhatt, M. Roy, S. Ahmad, A. Singh, M. Navaneethan, Y. Hayakawa, D. K. Aswal and S. K. Gupta, *J. Mater. Chem. A*, 2014, **2**, 6922–6930.

41 S. Bathula, M. Jayasimhadri, N. Singh, A. K. Srivastava, J. Pulikkotil, A. Dhar and R. C. Budhani, *Appl. Phys. Lett.*, 2012, **101**, 213902.

42 X. Chen, H. Zhang, Y. Zhao, W.-D. Liu, W. Dai, T. Wu, X. Lu, C. Wu, W. Luo, Y. Fan, L. Wang, W. Jiang, Z.-G. Chen and J. Yang, *ACS Appl. Mater. Interfaces*, 2019, **11**, 22457–22463.

43 R. Mulla, D. R. Jones and C. W. Dunnill, *ACS Sustainable Chem. Eng.*, 2020, **8**, 14234–14242.

44 Z. Lin, C. Hollar, J. S. Kang, A. Yin, Y. Wang, H.-Y. Shiu, Y. Huang, Y. Hu, Y. Zhang and X. Duan, *Adv. Mater.*, 2017, **29**, 1606662.

45 Y. He, T. Zhang, X. Shi, S.-H. Wei and L. Chen, *NPG Asia Mater.*, 2015, **7**, e210.

46 M. Li, Y. Liu, Y. Zhang, X. Han, T. Zhang, Y. Zuo, C. Xie, K. Xiao, J. Arbiol, J. Llorca, M. Ibáñez, J. Liu and A. Cabot, *ACS Nano*, 2021, **15**, 4967–4978.

47 Y. Zhang, C. Xing, Y. Liu, M. C. Spadaro, X. Wang, M. Li, K. Xiao, T. Zhang, P. Guardia, K. H. Lim, A. O. Moghaddam, J. Llorca, J. Arbiol, M. Ibáñez and A. Cabot, *Nano Energy*, 2021, **85**, 105991.

48 J.-A. Dolyniuk, B. Owens-Baird, J. Wang, J. V. Zaikina and K. Kovnir, *Mater. Sci. Eng., R*, 2016, **108**, 1–46.

49 M. Rull-Bravo, A. Moure, J. F. Fernández and M. Martín-González, *RSC Adv.*, 2015, **5**, 41653–41667.

50 Vikram, J. Kangsabanik, Enamullah and A. Alam, *J. Mater. Chem. A*, 2017, **5**, 6131–6139.

51 J. Ma, A. S. Nissimagoudar, S. Wang and W. Li, *Phys. Status Solidi RRL*, 2020, **14**, 2000084.

52 J.-H. Bahk, P. Santhanam, Z. Bian, R. Ram and A. Shakouri, *Appl. Phys. Lett.*, 2012, **100**, 012102.

53 Y. Zhang and G. D. Stucky, *Chem. Mater.*, 2014, **26**, 837–848.

54 L. Carbone and P. D. Cozzoli, *Nano Today*, 2010, **5**, 449–493.

55 M. Casavola, R. Buonsanti, G. Caputo and P. D. Cozzoli, *Eur. J. Inorg. Chem.*, 2008, 837–854.

56 J.-S. Lee, E. V. Shevchenko and D. V. Talapin, *J. Am. Chem. Soc.*, 2008, **130**, 9673–9675.

57 H. Xie, K. Wang, Y. Li, F. Zhao, Y. Ye, W. Ye and W. Ni, *Adv. Opt. Mater.*, 2021, 2002136.

58 X. Yin, L. Yang and Q. Gao, *Nanoscale*, 2020, **12**, 15944–15969.

59 K. Zhang, N. Xu, M. Jia, R. Li and M. Huang, *J. Appl. Phys.*, 2019, **125**, 183101.

60 S. Kulkarni, M. Jadhav, P. Raikar, S. Raikar and U. Raikar, *Ind. Eng. Chem. Res.*, 2019, **58**, 3630–3639.

61 Z. Li, L. Sun, Y. Liu, L. Zhu, D. Yu, Y. Wang, Y. Sun and M. Yu, *Environ. Sci.: Nano*, 2019, **6**, 1507–1515.

62 X. Li, G.-Q. Han, Y.-R. Liu, B. Dong, W.-H. Hu, X. Shang, Y.-M. Chai and C.-G. Liu, *ACS Appl. Mater. Interfaces*, 2016, **8**, 20057–20066.

63 E. P. Ferreira-Neto, S. Ullah, V. P. Martinez, J. M. S. C. Yabarrena, M. B. Simões, A. P. Perissinotto, H. Wender, F. S. de Vicente, P.-L. M. Noeske, S. J. L. Ribeiro and U. P. Rodrigues-Filho, *Mater. Adv.*, 2021, **2**, 2085–2096.

64 B.-M. Nguyen, Y. Taur, S. T. Picraux and S. A. Dayeh, *Nano Lett.*, 2014, **14**, 585–591.

65 M. Shaygan, K. Davami, B. Jin, T. Gemming, J.-S. Lee and M. Meyyappan, *J. Mater. Chem. C*, 2016, **4**, 2040–2046.

66 C. K. K. Choi, Y. T. E. Chiu, X. Zhuo, Y. Liu, C. Y. Pak, X. Liu, Y.-L. S. Tse, J. Wang and C. H. J. Choi, *ACS Nano*, 2019, **13**, 5864–5884.

67 M. L. Yola, N. Atar and N. Özcan, *Nanoscale*, 2021, **13**, 4660–4669.

68 S. Kulkarni, M. Jadhav, P. Raikar, D. A. Barretto, S. K. Vootla and U. S. Raikar, *New J. Chem.*, 2017, **41**, 9513–9520.

69 C. E. Marvinney, X. Shen, J. R. McBride, D. Critchlow, Z. Li, D. C. Mayo, R. R. Mu, S. T. Pantelides and R. F. Haglund, *ChemNanoMat*, 2018, **4**, 291–300.

70 L. Protesescu, T. Zünd, M. I. Bodnarchuk and M. V. Kovalenko, *ChemPhysChem*, 2016, **17**, 670–674.

71 D. Yanover, R. Vaxenburg, J. Tilchin, A. Rubin-Brusilovski, G. Zaiats, R. K. Čapek, A. Sashchiuk and E. Lifshitz, *J. Phys. Chem. C*, 2014, **118**, 17001–17009.

72 Z. Li, Y. Zhang and S. Jiang, *Adv. Mater.*, 2008, **20**, 4765–4769.

73 G. Park, C. Lee, D. Seo and H. Song, *Langmuir*, 2012, **28**, 9003–9009.

74 Z. Zhou, Z. Zhang, Q. Zhang, H. Yang, Y. Zhu, Y. Wang and L. Chen, *ACS Appl. Mater. Interfaces*, 2020, **12**, 1567–1576.

75 A. Samadi and S. Pourahmad, *Int. J. Energy Res.*, 2020, **44**, 10087–10100.

76 U. Sanyal, S. Ener, E. Anagnostopoulou, M. Pousthomis, P.-F. Fazzini, L.-M. Lacroix, K. P. Skokov, O. Gutfleisch and G. Viau, *Chem. Mater.*, 2016, **28**, 4982–4990.

77 L. Wang, C. Clavero, Z. Huba, K. J. Carroll, E. E. Carpenter, D. Gu and R. A. Lukaszew, *Nano Lett.*, 2011, **11**, 1237–1240.

78 L. Wang, K. Yang, C. Clavero, A. J. Nelson, K. J. Carroll, E. E. Carpenter and R. A. Lukaszew, *J. Appl. Phys.*, 2010, **107**, 09B303.

79 W. Zhang, L. Wu, J. Du, J. Tian, Y. Li, Y. Zhao, H. Wu, Y. Zhong, Y.-C. Cao and S. Cheng, *Mater. Adv.*, 2021, **2**, 4634–4642.

80 H.-p. Feng, L. Tang, G.-m. Zeng, Y. Zhou, Y.-c. Deng, X. Ren, B. Song, C. Liang, M.-y. Wei and J.-f. Yu, *Adv. Colloid Interface Sci.*, 2019, **267**, 26–46.

81 Y. Cao, M. Bernechea, A. Maclachlan, V. Zardetto, M. Creatore, S. A. Haque and G. Konstantatos, *Chem. Mater.*, 2015, **27**, 3700–3706.

82 M.-Y. Lu, M.-H. Hong, Y.-M. Ruan and M.-P. Lu, *Chem. Commun.*, 2019, **55**, 5351–5354.

83 C. M. Pelicano, I. Raifuku, Y. Ishikawa, Y. Uraoka and H. Yanagi, *Mater. Adv.*, 2020, **1**, 1253–1261.

84 V. Hiremath, M. L. T. Trivino, R. Shavi, M. N. Gebresillase and J. G. Seo, *Mater. Lett.*, 2018, **211**, 304–307.

85 N. Ali, A. A. Babar, Y. Zhang, N. Iqbal, X. Wang, J. Yu and B. Ding, *J. Colloid Interface Sci.*, 2020, **560**, 379–387.

86 T. K. Kim, K. J. Lee, J. Yuh, S. K. Kwak and H. R. Moon, *New J. Chem.*, 2014, **38**, 1606–1610.

87 Y. Jang, A. Shapiro, M. Isarov, A. Rubin-Brusilovski, A. Safran, A. K. Budniak, F. Horani, J. Dehnel, A. Sashchiuk and E. Lifshitz, *Chem. Commun.*, 2017, **53**, 1002–1024.

88 R. Mastria and A. Rizzo, *J. Mater. Chem. C*, 2016, **4**, 6430–6446.

89 G. S. Selopal, H. Zhao, Z. M. Wang and F. Rosei, *Adv. Funct. Mater.*, 2020, **30**, 1908762.

90 M. Scheele, N. Oeschler, I. Veremchuk, S.-O. Peters, A. Littig, A. Kornowski, C. Klinke and H. Weller, *ACS Nano*, 2011, **5**, 8541–8551.

91 M. Wagner, G. Span, S. Holzer, O. Triebl, T. Grasser and V. Palankovski, *ECS Trans.*, 2019, **3**, 1151–1162.

92 G. J. Snyder and E. S. Toberer, *Nat. Mater.*, 2008, **7**, 105–114.

93 X. Li, C. Hu, X. Kang, Q. Len, Y. Xi, K. Zhang and H. Liu, *J. Mater. Chem. A*, 2013, **1**, 13721–13726.

94 L. Wu, X. Li, S. Wang, T. Zhang, J. Yang, W. Zhang, L. Chen and J. Yang, *NPG Asia Mater.*, 2017, **9**, e343.

95 J. P. Heremans, V. Jovovic, E. S. Toberer, A. Saramat, K. Kurosaki, A. Charoenphakdee, S. Yamanaka and G. J. Snyder, *Science*, 2008, **321**, 554.

96 F. Serrano-Sánchez, T. Luo, J. Yu, W. Xie, C. Le, G. Auffermann, A. Weidenkaff, T. Zhu, X. Zhao, J. A. Alonso, B. Gault, C. Felser and C. Fu, *J. Mater. Chem. A*, 2020, **8**, 14822–14828.

97 Z.-G. Chen, G. Han, L. Yang, L. Cheng and J. Zou, *Prog. Nat. Sci.: Mater. Int.*, 2012, **22**, 535–549.

98 S. S. Kubakaddi and B. G. Mulimani, *J. Appl. Phys.*, 1985, **58**, 3643–3645.

99 J. Sun, M. L. Yeh, B. J. Jung, B. Zhang, J. Feser, A. Majumdar and H. E. Katz, *Macromolecules*, 2010, **43**, 2897–2903.

100 Z. Ma, C. Wang, J. Lei, D. Zhang, Y. Chen, Y. Wang, J. Wang and Z. Cheng, *Nanoscale*, 2020, **12**, 1904–1911.

101 H.-Z. Li, R.-P. Li, J.-H. Liu and M.-J. Huang, *Phys. B: Condensed Matter*, 2015, **479**, 1–5.

102 Y. Min, J. W. Roh, H. Yang, M. Park, S. I. Kim, S. Hwang, S. M. Lee, K. H. Lee and U. Jeong, *Adv. Mater.*, 2013, **25**, 1425–1429.

103 Y. Zheng, Y. Luo, C. Du, B. Zhu, Q. Liang, H. H. Hng, K. Hippalgaonkar, J. Xu and Q. Yan, *Mater. Chem. Front.*, 2017, **1**, 2457–2473.

104 P. G. Burke, B. M. Curtin, J. E. Bowers and A. C. Gossard, *Nano Energy*, 2015, **12**, 735–741.

105 Y. Luo, Q. Jiang, J. Yang, W. Li, D. Zhang, Z. Zhou, Y. Cheng, Y. Ren, X. He and X. Li, *Nano Energy*, 2017, **32**, 80–87.

106 S. J. Poon, A. S. Petersen and D. Wu, *Appl. Phys. Lett.*, 2013, **102**, 173110.

107 M. Ibáñez, R. Zamani, S. Gorsse, J. Fan, S. Ortega, D. Cadavid, J. R. Morante, J. Arbiol and A. Cabot, *ACS Nano*, 2013, **7**, 2573–2586.

108 M. Ibáñez, R. J. Korkosz, Z. Luo, P. Riba, D. Cadavid, S. Ortega, A. Cabot and M. G. Kanatzidis, *J. Am. Chem. Soc.*, 2015, **137**, 4046–4049.

109 R. Miranti, D. Shin, R. D. Septianto, M. Ibáñez, M. V. Kovalenko, N. Matsushita, Y. Iwasa and S. Z. Bisri, *ACS Nano*, 2020, **14**, 3242–3250.

110 C. Ou, J. Hou, T.-R. Wei, B. Jiang, S. Jiao, J.-F. Li and H. Zhu, *NPG Asia Mater.*, 2015, **7**, e182.

111 Y. Jin, J. Hwang, M.-K. Han, W. Shon, J.-S. Rhyee and S.-J. Kim, *ACS Appl. Mater. Interfaces*, 2020, **12**, 36589–36599.

112 V. Sharma, G. S. Okram, D. Verma, N. P. Lalla and Y.-K. Kuo, *ACS Appl. Mater. Interfaces*, 2020, **12**, 54742–54751.

113 M. Ibáñez, R. Hasler, Y. Liu, O. Dobrozhan, O. Nazarenko, D. Cadavid, A. Cabot and M. V. Kovalenko, *Chem. Mater.*, 2017, **29**, 7093–7097.

114 J. Moon, J.-H. Kim, Z. C. Y. Chen, J. Xiang and R. Chen, *Nano Lett.*, 2013, **13**, 1196–1202.

115 X. Chen, Y. Wang and Y. Ma, *J. Phys. Chem. C*, 2010, **114**, 9096–9100.

116 Z.-H. Ge, P. Qin, D. He, X. Chong, D. Feng, Y.-H. Ji, J. Feng and J. He, *ACS Appl. Mater. Interfaces*, 2017, **9**, 4828–4834.

117 T. Juntunen, T. Koskinen, V. Khayrudinov, T. Haggren, H. Jiang, H. Lipsanen and I. Tittonen, *Nanoscale*, 2019, **11**, 20507–20513.

118 M. C. Wingert, Z. C. Y. Chen, E. Dechaumphai, J. Moon, J.-H. Kim, J. Xiang and R. Chen, *Nano Lett.*, 2011, **11**, 5507–5513.

119 J.-N. Shen, L.-M. Wu and Y.-F. Zhang, *J. Mater. Chem. A*, 2014, **2**, 2538–2543.

120 Y. Wang, B. Li and G. Xie, *RSC Adv.*, 2013, **3**, 26074–26079.

121 K. Yang, A. Cantarero, A. Rubio and R. D'Agosta, *Nano Res.*, 2015, **8**, 2611–2619.

122 M. Hu, K. P. Giapis, J. V. Goicochea, X. Zhang and D. Poulikakos, *Nano Lett.*, 2011, **11**, 618–623.

123 S. Fust, A. Faustmann, D. J. Carrad, J. Bissinger, B. Loitsch, M. Döblinger, J. Becker, G. Abstreiter, J. J. Finley and G. Koblmüller, *Adv. Mater.*, 2020, **32**, 1905458.

124 J. Kang, J. W. Roh, W. Shim, J. Ham, J.-S. Noh and W. Lee, *Adv. Mater.*, 2011, **23**, 3414–3419.

125 G. Zhang, W. Wang and X. Li, *Adv. Mater.*, 2008, **20**, 3654–3656.

126 M. Kockert, R. Mitdank, H. Moon, J. Kim, A. Mogilatenko, S. H. Moosavi, M. Kroener, P. Woias, W. Lee and S. F. Fischer, *Nanoscale Adv.*, 2021, **3**, 263–271.

127 S. Hong, W. Kim, S.-J. Jeon, S. C. Lim, H.-J. Lee, S. Hyun, Y. H. Lee and S. Baik, *J. Phys. Chem. C*, 2013, **117**, 913–917.

128 B. Ketharachapalli and R. K. Dash, *Appl. Nanosci.*, 2018, **8**, 1887–1893.

129 J. Xiang, W. Lu, Y. Hu, Y. Wu, H. Yan and C. M. Lieber, *Nature*, 2006, **441**, 489–493.

130 P. Ying, R. He, J. Mao, Q. Zhang, H. Reith, J. Sui, Z. Ren, K. Nielsch and G. Schierning, *Nat. Commun.*, 2021, **12**, 1121.

131 R. Mulla, D. R. Jones and C. W. Dunnill, *Mater. Today Commun.*, 2021, **29**, 102738.

132 G. Dennler, R. Chmielowski, S. Jacob, F. Capet, P. Roussel, S. Zastrow, K. Nielsch, I. Opahle and G. K. H. Madsen, *Adv. Energy Mater.*, 2014, **4**, 1301581.

133 R. Mulla and M. K. Rabinal, *Ultrason. Sonochem.*, 2017, **39**, 528–533.

134 Y. Wu, Q. Lou, Y. Qiu, J. Guo, Z.-Y. Mei, X. Xu, J. Feng, J. He and Z.-H. Ge, *Inorg. Chem. Front.*, 2019, **6**, 1374–1381.

135 C. J. Barnett, J. E. McCormack, E. M. Deemer, C. R. Evans, J. E. Evans, A. O. White, P. R. Dunstan, R. R. Chianelli, R. J. Cobley and A. R. Barron, *J. Phys. Chem. C*, 2020, **124**, 18777–18783.

136 C. J. Barnett, J. D. McGettrick, V. S. Gangoli, E. Kazimierska, A. Orbaek White and A. R. Barron, *Materials*, 2021, **14**, 2106.

137 B. Kumanek, G. Stando, P. Stando, K. Matuszek, K. Z. Milowska, M. Krzywiecki, M. Gryglas-Borysiewicz, Z. Ogorzałek, M. C. Payne, D. MacFarlane and D. Janas, *Sci. Rep.*, 2021, **11**, 8649.

138 H. R. Lee, N. Furukawa, A. J. Ricco, E. Pop, Y. Cui and Y. Nishi, *Appl. Phys. Lett.*, 2021, **118**, 173901.

139 R. Nunna, P. Qiu, M. Yin, H. Chen, R. Hanus, Q. Song, T. Zhang, M.-Y. Chou, M. T. Agne, J. He, G. J. Snyder, X. Shi and L. Chen, *Energy Environ. Sci.*, 2017, **10**, 1928–1935.

140 F. L. De Volder Michael, H. Tawfick Sameh, H. Baughman Ray and A. J. Hart, *Science*, 2013, **339**, 535–539.

141 J. L. Blackburn, A. J. Ferguson, C. Cho and J. C. Grunlan, *Adv. Mater.*, 2018, **30**, 1704386.

142 T. Lee, J. W. Lee, K. T. Park, J.-S. Kim, C. R. Park and H. Kim, *ACS Nano*, 2021, **15**, 13118–13128.

143 K. T. Park, T. Lee, Y. Ko, Y. S. Cho, C. R. Park and H. Kim, *ACS Appl. Mater. Interfaces*, 2021, **13**, 6257–6264.

144 Y. Wang, Z. Lu, Q. Hu, X. Qi, Q. Li, Z. Wu, H.-L. Zhang, C. Yu and H. Wang, *J. Mater. Chem. A*, 2021, **9**, 3341–3352.

145 M. S. Islam, H. Ohmagari, M. A. Rahman, Y. Shudo, M. Fukuda, J. Yagyu, Y. Sekine, L. F. Lindoy and S. Hayami, *Mater. Adv.*, 2021, **2**, 5645–5649.

146 W.-H. Chiang, C.-Y. Hsieh, S.-C. Lo, Y.-C. Chang, T. Kawai and Y. Nonoguchi, *Carbon*, 2016, **109**, 49–56.

147 K. Xu, G. Chen and D. Qiu, *J. Mater. Chem. A*, 2013, **1**, 12395–12399.

148 S. Han, W. Zhai, G. Chen and X. Wang, *RSC Adv.*, 2014, **4**, 29281–29285.

149 X. Hu, G. Chen and X. Wang, *Compos. Sci. Technol.*, 2017, **144**, 43–50.

150 C. Gao and G. Chen, *Small*, 2018, **14**, 1703453.

151 Y. Xue, Z. Zhang, Y. Zhang, X. Wang, L. Li, H. Wang and G. Chen, *Carbon*, 2020, **157**, 324–329.

152 Y. Xue, C. Gao, L. Liang, X. Wang and G. Chen, *J. Mater. Chem. A*, 2018, **6**, 22381–22390.

153 T. J. Slade, S. Anand, M. Wood, J. P. Male, K. Imasato, D. Cheikh, M. M. Al Malki, M. T. Agne, K. J. Griffith, S. K. Bux, C. Wolverton, M. G. Kanatzidis and G. J. Snyder, *Joule*, 2021, **5**, 1168–1182.

154 R. Mulla and M. H. K. Rabinal, *Energy Technol.*, 2019, **7**, 1800850.

155 Y. Li, Z. Wu, J. Lin, Y. Wang, J. Mao, H. Xie and Z. Li, *Mater. Sci. Semicond. Process.*, 2021, **121**, 105393.

156 M. Liu and X. Y. Qin, *Appl. Phys. Lett.*, 2012, **101**, 132103.

157 D. Ginting, C.-C. Lin, L. Rathnam, J. H. Yun, B.-K. Yu, S.-J. Kim and J.-S. Rhyee, *J. Mater. Chem. A*, 2017, **5**, 13535–13543.

158 B. Paul, A. K. Vaddepally and P. Banerji, *J. Appl. Phys.*, 2010, **108**, 064322.

159 P. K. Rawat, B. Paul and P. Banerji, *ACS Appl. Mater. Interfaces*, 2014, **6**, 3995–4004.

160 S. Li, J. Xin, A. Basit, Q. Long, S. Li, Q. Jiang, Y. Luo and J. Yang, *Adv. Sci.*, 2020, **7**, 1903493.

161 M. Yaprintsev, A. Vasil'ev, O. Ivanov, M. Zhezhu, E. Yaprintseva and V. Novikov, *Scr. Mater.*, 2021, **194**, 113710.

162 S. Cai, S. Hao, Z.-Z. Luo, X. Li, I. Hadar, T. P. Bailey, X. Hu, C. Uher, Y.-Y. Hu, C. Wolverton, V. P. Dravid and M. G. Kanatzidis, *Energy Environ. Sci.*, 2020, **13**, 200–211.

163 B. Xiang, J. Liu, J. Yan, M. Xia, Q. Zhang, L. Chen, J. Li, X. Y. Tan, Q. Yan and Y. Wu, *J. Mater. Chem. A*, 2019, **7**, 18458–18467.

164 J. Zhang, S. Li, Z. Zhu, Z. Wu and J. Zhang, *Dalton Trans.*, 2021, **50**, 10515–10523.

165 Y.-X. Zhang, Z.-H. Ge and J. Feng, *J. Alloys Compd.*, 2017, **727**, 1076–1082.

166 Y.-X. Zhang, Y.-K. Zhu, D.-S. Song, J. Feng and Z.-H. Ge, *Chem. Commun.*, 2021, **57**, 2555–2558.

167 X. Meng, Z. Liu, B. Cui, D. Qin, H. Geng, W. Cai, L. Fu, J. He, Z. Ren and J. Sui, *Adv. Energy Mater.*, 2017, **7**, 1602582.

168 P.-a. Zong, R. Hanus, M. Dylla, Y. Tang, J. Liao, Q. Zhang, G. J. Snyder and L. Chen, *Energy Environ. Sci.*, 2017, **10**, 183–191.

169 P.-a. Zong, X. Chen, Y. Zhu, Z. Liu, Y. Zeng and L. Chen, *J. Mater. Chem. A*, 2015, **3**, 8643–8649.

170 U. G. Hwang, K. Kim, W. Kim, W. H. Shin, W.-S. Seo and Y. S. Lim, *Electron. Mater. Lett.*, 2019, **15**, 605–612.

171 J. U. Rahman, N. V. Du, W. H. Nam, W. H. Shin, K. H. Lee, W.-S. Seo, M. H. Kim and S. Lee, *Sci. Rep.*, 2019, **9**, 8624.

172 L. Chen, W. Zhao, M. Li, G. Yang, S. M. K. Nazrul Islam, D. R. G. Mitchell, Z. Cheng and X. Wang, *Nanoscale*, 2020, **12**, 12760–12766.

173 B. F. Machado and P. Serp, *Catal. Sci. Technol.*, 2012, **2**, 54–75.

174 R. M. Gunnagol and M. H. K. Rabinal, *ChemistrySelect*, 2018, **3**, 2578–2585.

175 R. Li, S. Wang, P. Bai, B. Fan, B. Zhao and R. Zhang, *Mater. Adv.*, 2021, **2**, 718–727.

176 B. Sharma, R. Mulla and M. K. Rabinal, *AIP Conf. Proc.*, 2015, **1665**, 050129.

177 S. Nandhini and G. Muralidharan, *Electrochim. Acta*, 2021, **365**, 137367.

178 G. N. S. Babu and N. Kalaiselvi, *Electrochim. Acta*, 2021, **372**, 137855.

179 S. N. Prashanth, N. L. Teradal, J. Seetharamappa, A. K. Satpati and A. V. R. Reddy, *Electrochim. Acta*, 2014, **133**, 49–56.

180 N. Shauloff, N. L. Teradal and R. Jelinek, *ACS Sens.*, 2020, **5**, 1573–1581.

181 B. Feng, J. Xie, G. Cao, T. Zhu and X. Zhao, *J. Mater. Chem. A*, 2013, **1**, 13111–13119.

182 L. Huang, J. Lu, D. Ma, C. Ma, B. Zhang, H. Wang, G. Wang, D. H. Gregory, X. Zhou and G. Han, *J. Mater. Chem. A*, 2020, **8**, 1394–1402.

183 P.-a. Zong, J. Liang, P. Zhang, C. Wan, Y. Wang and K. Koumoto, *ACS Appl. Energy Mater.*, 2020, **3**, 2224–2239.

184 J. Huang, P. Yan, Y. Liu, J. Xing, H. Gu, Y. Fan and W. Jiang, *ACS Appl. Mater. Interfaces*, 2020, **12**, 52721–52730.

185 J. Cao, D. Ekren, Y. Peng, F. Azough, I. A. Kinloch and R. Freer, *ACS Appl. Mater. Interfaces*, 2021, **13**, 11879–11890.

186 H. Tang, F.-H. Sun, J.-F. Dong, Asfandiyar, H.-L. Zhuang, Y. Pan and J.-F. Li, *Nano Energy*, 2018, **49**, 267–273.

187 Y. He, T. Day, T. Zhang, H. Liu, X. Shi, L. Chen and G. J. Snyder, *Adv. Mater.*, 2014, **26**, 3974–3978.

188 X. Liang, *Appl. Phys. Lett.*, 2017, **111**, 133902.

189 L. Fu, J. Yang, J. Peng, Q. Jiang, Y. Xiao, Y. Luo, D. Zhang, Z. Zhou, M. Zhang, Y. Cheng and F. Cheng, *J. Mater. Chem. A*, 2015, **3**, 1010–1016.

190 K.-C. Kim, S.-S. Lim, S. H. Lee, J. Hong, D.-Y. Cho, A. Y. Mohamed, C. M. Koo, S.-H. Baek, J.-S. Kim and S. K. Kim, *ACS Nano*, 2019, **13**, 7146–7154.

191 J. Hwang, H. Kim, M.-K. Han, J. Hong, J.-H. Shim, J.-Y. Tak, Y. S. Lim, Y. Jin, J. Kim, H. Park, D.-K. Lee, J.-H. Bahk, S.-J. Kim and W. Kim, *ACS Nano*, 2019, **13**, 8347–8355.

192 S. Ortega, M. Ibáñez, Y. Liu, Y. Zhang, M. V. Kovalenko, D. Cadavid and A. Cabot, *Chem. Soc. Rev.*, 2017, **46**, 3510–3528.

193 R. Mulla and M. K. Rabinal, *Energy Technol.*, 2018, **6**, 1178–1185.

194 C. Gayner and Y. Amouyal, *Adv. Funct. Mater.*, 2020, **30**, 1901789.